HHS Public Access

Author manuscript

Nature. Author manuscript; available in PMC 2023 May 01.

Published in final edited form as:

Nature. 2022 November ; 611(7934): 180–187. doi:10.1038/s41586-022-05373-x.

Bestrophin-2 and glutamine synthetase form a complex for glutamate release

Aaron P. Owji[1,2,#], **Kuai Yu**[3,#], **Alec Kittredge**[1,2,#], **Jiali Wang**[1,#], **Yu Zhang**[1,*], **Tingting Yang**[1,*]

[1]Department of Ophthalmology, Columbia University, New York, NY, USA

[2]Department of Pharmacology, Columbia University, New York, NY, USA

[3]Department of Cell Biology, Emory University, School of Medicine, Atlanta, GA, USA

Abstract

Bestrophin-2 (Best2) is a member of the bestrophin family of calcium-activated anion channels with critical involvement in ocular physiology[1–4]. Here, we uncover a directional permeability of Best2 to glutamate heavily favoring glutamate exit, identify glutamine synthetase (GS) as a binding partner of Best2 in the ciliary body of the eye, and solve the structure of the Best2-GS complex. Best2 reduces cytosolic GS activity by tethering GS to the cell membrane. GS extends the ion conducting pathway of Best2 through its central cavity and inhibits Best2 channel function in the absence of intracellular glutamate, but sensitizes Best2 to intracellular glutamate, which promotes opening of Best2 and thus relieves the inhibitory effect of GS. The physiological role of Best2 in conducting chloride and glutamate and the influence of GS are demonstrated in non-pigmented ciliary epithelial cells. Together, our results reveal a novel mechanism of glutamate release through Best2-GS.

Introduction

Bestrophins are a family of Ca^{2+}-activated anion channels broadly distributed in various types of epithelial and neuronal cells[2,5–7]. Among the four known bestrophin paralogs, bestrophin-2 (Best2) is highly expressed in ocular non-pigmented epithelium (NPE) of the ciliary body[1,4], and is involved in aqueous humor homeostasis, which ultimately determine intra-ocular pressure (IOP)[1,3]. Notably, knockout of Best2 in mice leads to a reduction of IOP[1,3], suggesting the potential of targeting Best2 and its regulators for relieving ocular hypertension, which is a common clinical phenotype and a risk factor for many eye diseases

[*]Correspondence: Tingting Yang, ty2190@cumc.columbia.edu, Yu Zhang, yz3802@cumc.columbia.edu.
[#]These authors contributed equally to this work

Author Contributions

A.P.O. designed research, performed protein purification and cryo-EM experiments, analyzed data, made figures and wrote the paper; K.Y. and J.W. designed research, performed patch clamp recordings, analyzed data and made figures; A.K. designed research, generated constructs, performed bovine ciliary lysate pull-down, immunoblotting and GS activity experiments, analyzed data, made figures, and helped write the paper; Y.Z. and T.Y. designed research, performed experiments, analyzed data, made figures and wrote the paper.

Competing Interests

The authors declare no conflict of interest.

including open-angle glaucoma[8–10]. Therefore, it is of tremendous biomedical value to understand Best2's interacting partners and permeability to physiological anions in NPE.

However, there are no proteins known to interact with Best2. In regard to anion permeability, Best2 has been shown to permeate F^-, Cl^-, Br^-, I^-, SCN^-, $CH_3SO_3^-$ and HCO_3^- in transiently expressed HEK293 cells[11–13], and suggested to conduct HCO_3^- in colon goblet cells and Cl^- in NPE cells[1,14], although the latter physiological role has not been directly demonstrated. Moreover, bestrophin-1 (Best1), another paralog in the bestrophin family, has been shown to conduct multiple important neurotransmitters in astrocytes, including glutamate, GABA and d-serine, which are much bigger in size compared to Cl^- and HCO_3^-[6,15–21]. Whether Best2 is permeable to these osmolytes is unknown, but both structural and functional data support this possibility: Best1 and Best2 have an overall conserved architecture with two major constrictions in the ion conducting pathway, namely the "neck" and "aperture", both of which open to a greater degree in Best2 than in Best1[11,22–25]; Best2 conducts significantly larger Cl^- currents compared to Best1 in transiently transfected HEK293 cells despite similar expression levels of the two paralogs[11,23]. As the anionic and main form of glutamic acid under physiological conditions, glutamate is the most abundant excitatory neurotransmitter in the human nervous system and can be directly converted to glutamine by glutamine synthetase (GS). However, there is no known or expected linkage between Best2 and any factor involved in glutamate metabolism.

Results

Best2-GS interaction in ciliary body

To identify Best2 interactors, we used previously purified bovine Best2 (bBest2)[11], which has 91% sequence identity with the human ortholog (hBest2). Ni^{2+} beads bound to bBest2-YFP-His were incubated with bovine ciliary body lysate to pull down the bBest2 interacting complex, followed by mass spectrometry. A top scorer was identified as glutamine synthetase (GS) (Extended Data Fig. 1), a key metabolic enzyme that catalyzes the ATP-dependent condensation of glutamate and ammonia to glutamine. Consistent with this finding, GS expression has been documented in NPE cells of the ciliary body[26,27], where Best2 resides. Furthermore, altered levels of glutamate/glutamine and GS activity have been reported in high IOP and glaucoma models[28,29], implicating a functional crosstalk between Best2 and GS in IOP regulation.

To validate the Best2-GS interaction, CFP-Myc tagged bovine and human GS (bGS and hGS, respectively), which share 96% sequence identity, were individually co-transfected with YFP-His tagged Best2 from the same species into HEK293 cells. Lysates were immunoprecipitated with a Myc antibody and immunoblotted with a GFP antibody that recognizes both CFP and YFP. Both bovine and human Best2 were co-immunoprecipitated with GS (Fig. 1a and Extended Data Fig. 2a), confirming the Best2-GS interaction in both species. These data demonstrate a novel and conserved Best2-GS interaction in mammals.

Cryo-EM structure of Best2-GS

To investigate the structural basis of this interaction, bGS and bBest2 were separately purified and mixed on ice for 60 min prior to cryo-EM grid preparation. By single-particle cryo-EM, the bBest2-GS co-structure was solved at 2.0 Å (Fig. 1b, c, Extended Data Fig. 3 and Extended Data Table 1). Each bBest2-GS complex is formed by a bBest2 pentamer bound to one face of a bGS decamer, which is composed of two pentamers aligned back-to-back (Fig. 1b, c). Remarkably, the exposed pentameric surface of bGS binds to the cytosolic surface of pentameric bBest2, such that the two proteins share the C5 symmetry axis and the ion-conducting pore of bBest2 extends into the central cavity of bGS (Fig. 1b, c and Extended Data Fig. 4a–d). In this co-structure, bBest2 is in the closed state while bGS is in the apo state, with no substantial conformational change in either component compared to previously reported structures: the root-mean-square deviation (RMSD) is 0.35 Å for bBest2 (compared to PDB 6VX7, bBest2 in the closed state) and 0.43 Å for bGS (compared to PDB 2UU7, canine GS in the apo state)[11,30].

The binding interface of the bBest2-GS complex comprises ~1746 $Å^2$. A single conserved arginine, R197, located on the surface of the cytosolic vestibule of bBest2, binds the backbone carbonyl of G23 (Fig. 1d), situated on a loop between the first alpha helix and first beta sheet of bGS (Extended Data Fig. 4e, f). G23 is located immediately before the beta grasp domain, which comprises residues 25–112 (Fig. 1d and Extended Data Fig. 4e, f). Besides this direct contact, a salt bridge is formed between the side chain nitrogen of bGS K52 situated on the beta grasp domain and the backbone carbonyl oxygen of bBest2 D327 in the cytosolic domain (Fig. 1e). Notably, these residues are all highly conserved among Best2 and GS homologs, supporting the biological significance of the Best2-GS interaction.

GS inhibits Best2 channel function

To probe the functional consequences of the Best2-GS interaction on Best2 channel, hBest2 was transfected with or without hGS into HEK293 cells, and the Ca^{2+}-dependent Cl^- currents were measured by whole-cell patch clamp across a range of free intracellular Ca^{2+} concentrations ($[Ca^{2+}]_i$). From cells expressing hBest2 alone, a plot of peak current (evoked with a +100 mV step pulse) as a function of $[Ca^{2+}]_i$ displayed robust Ca^{2+}-dependent activation with the Ca^{2+} half-maximal effective concentration (EC_{50}) at 330 nM (Fig. 2a), which is comparable to that of mBest2[12]. The EC_{50} measured from cells co-expressing hBest2 and hGS is similar to that of hBest2 alone (Fig. 2b), indicating that hGS does not affect the Ca^{2+} sensitivity of hBest2. On the other hand, the current amplitudes from cells co-expressing hBest2 and hGS were significantly smaller compared to cells expressing hBest2 alone at all tested $[Ca^{2+}]_i$s (Fig. 2b–d and Extended Data Fig. 5a), indicating a negative influence of hGS on hBest2 channel function. Consistently, the current amplitudes from cells co-expressing bBest2 and bGS were significantly smaller compared to those from cells expressing bBest2 alone at 1 μM $[Ca^{2+}]_i$ (peak current, Fig. 2e, f). The overall and membrane-bound protein levels of Best2 were unaltered upon GS co-transfection (Fig. 3a and Extended Data Fig. 2a, b), suggesting that GS does not inhibit Best2 by reducing the protein expression or membrane localization of Best2.

HEK293 cells endogenously express hGS[31], which potentially presents an undesired background for analyzing the influence of GS on Best2 after heterologous expression in these cells. However, the protein level of exogenous hGS was overwhelmingly higher than that of the endogenous hGS (Extended Data Fig. 2c), suggesting that the background hGS is negligible for functional analyses.

Best2 reduces cytosolic GS activity

To probe the impact of Best2, which is a membrane protein, on the subcellular localization of GS, we performed immunoblotting after subcellular fractionation of lysates from HEK293 cells transfected with hBest2 alone, hGS alone or hGS + hBest2. In the absence of hBest2, hGS was not detected in the membrane fraction, whereas in the presence of hBest2, a portion of hGS was detected in the membrane fractions along with reduced cytosolic distribution despite an unaltered overall expression level (Fig. 3a and Extended Data Fig. 2b). Consistently, when the cellular GS activity was measured by a colorimetric assay, cells co-expressing hGS and hBest2 exhibited lower cytosolic GS activity compared to cells expressing hGS alone (Fig. 3b), while the overall GS activity in whole-cell lysate was not affected by the presence of hBest2 (Extended Data Fig. 6a). As bGS binds to the cytosolic side of bBest2 in the co-structure (Fig. 1c), these results suggest that Best2 reduces the cytosolic level of GS by tethering a fraction of GS to the cell membrane.

To further investigate whether Best2 directly influences GS enzyme activity in the Best2-GS complex, we performed the colorimetric GS activity assay with purified bBest2 and bGS, such that the protein's subcellular localization is no longer a factor. The catalytic activity of bGS was unaltered by pre-mixing with bBest2 at different ratios (Fig. 3c), suggesting that the intrinsic enzyme activity of bGS was not affected by bBest2 in the bBest2-GS complex. Consistent with these functional results, the GS active site is situated at the interface of the beta grasp domain and the catalytic domain of two adjacent protomers, such that the Best2-GS interaction does not sterically occlude the solvent or substrate access to the active site (Extended Data Fig. 4a, e, f). Additionally, the small conformational change induced by substrate binding (ATP/ADP) in the catalytic and beta grasp domains should not be affected by Best2[30].

To test whether Best2's channel activity is involved in membrane-tethering of GS, we individually introduced two hBest2 mutations, G299A and D304A, which are located in the Ca^{2+}-binding clasp and thus predicted to be structurally stable but functionally deficient due to disrupted binding of the essential activator Ca^{2+}[32,33]. Both mutants were expressed at a similar level to WT hBest2 but conducted negligible currents in transiently transfected HEK293 cells (Fig. 3a, d), confirming their functional deficiency. When co-expressed with hGS, both G299A and D304A mutants resembled WT hBest2 in terms of interacting with hGS and reducing the cytosolic expression level of hGS by tethering hGS to the membrane (Fig. 3a and Extended Data Fig. 2a, d). Therefore, Best2 channel activity is not required for the Best2-GS interaction and membrane-tethering of GS.

Key residues at the Best2-GS interface

To examine the contributions of residues at the Best2-GS interacting interface, we generated four single alanine substitution mutants, namely R197A and D327A in hBest2, and G23A and K52A in hGS. When each mutant and the WT binding partner were co-transfected into HEK293 cells, the protein expression was unaltered but the co-immunoprecipitation was severely diminished (Extended Data Fig. 2a). As a complementary approach, we used fluorescence resonance energy transfer (FRET) to probe the interaction between Venus-tagged hBest2 and Cerulean-tagged hGS constructs (Extended Data Fig. 6b)[34]. All WT-mutant pairs showed a significant decrease (6 to 19 fold) in the relative binding affinity ($K_{d,EFF}^{-1}$) compared to the WT-WT pair (Extended Data Fig. 6b), confirming the important roles of these residues in mediating the Best2-GS interaction.

The G23A and K52A mutants of hGS both exhibited WT-like overall and cytosolic activity which was not affected by the presence of hBest2 in transiently transfected HEK293 cells (Extended Data Fig. 6a, c), indicating their catalytic integrity and the non-involvement of hBest2 in the regulation of their activity. Importantly, neither of them inhibited hBest2-mediated currents (Extended Data Fig. 6d), while only a tiny fraction of the hGS mutant proteins were detected in the membrane fraction (Extended Data Fig. 2d). These results establish an essential requirement of the physical interaction between Best2 and GS for their mutual influences.

Best2 directionally conducts glutamate

As glutamate is the substrate of GS and an anion, we wondered if it could be conducted by Best2. To test this idea, we performed patch clamp with glutamate as the principal anion in both internal and external solutions. Robust Ca^{2+}-dependent glutamate currents were recorded in HEK293 cells transiently expressing hBest2 (Fig. 4a, grey and black), indicating that hBest2 is permeable to glutamate. To measure the relative permeability of glutamate to Cl^-, currents from hBest2 were recorded with glutamate and Cl^- each present in one side of the patch solutions. Strikingly, the relative location of the anions had a substantial influence on hBest2-mediated currents. With internal glutamate and external Cl^-, the reversal potential was slightly left shifted (E_{rev} = −14.8 ± 2.1 mV, Fig. 4b, black, and Extended Data Fig. 7a) and the permeability ratio of glutamate in relative to Cl^- (P_{Glu}/P_{Cl}) was 0.56 (Fig. 4c). In sharp contrast, with external glutamate and internal Cl^-, the reversal potential shifted significantly to the right (E_{rev} = 50.7 ± 3.9 mV, Fig. 4d, black, and Extended Data Fig. 7b), and P_{Glu}/P_{Cl} was 0.08 (Fig. 4e). These results indicate that hBest2 is much more permeable to intracellular (internal) glutamate than extracellular (external) glutamate.

Moreover, substituting Cl^- in the internal solution with glutamate resulted in a strong increase of not only inward current (glutamate efflux) but also outward current (Cl^- influx) from hBest2 (Fig. 4b, f and Extended Data Fig. 5b), indicating that glutamate on the intracellular side of the channel promotes Cl^- inward movement from the extracellular side in *trans*. In sharp contrast, placing glutamate in the external solution did not have this *trans* promotive effect (Fig. 4d, f and Extended Data Fig. 5c). As the *trans* effect reflects influence on channel gating, these results suggest that glutamate induces opening of hBest2 specifically from the intracellular/cytosolic side of the channel. Then, we performed patch

clamp analysis with different concentrations of glutamate substituting Cl^- in the internal solution. The plot of P_{Glu}/P_{Cl} was fitted to the Hill equation, and the EC_{50} concentration of intracellular glutamate required for activating hBest2 was measured as 46 mM (Extended Data Fig. 8a, b).

Taken together, our results demonstrate a directional permeability of hBest2 to glutamate, which underlies a potential physiological role of Best2 in releasing intracellular glutamate while prohibiting extracellular glutamate from entering the cell (Fig. 4j).

GS sensitizes Best2 to intracellular Glu

We then examined the influence of GS on Best2's glutamate permeability. When Cl^- and glutamate were the principal anion in the internal and external solution, respectively, both the inward (Cl^-) and outward (glutamate) currents from hBest2 were significantly decreased in the presence of hGS compared to those in the absence of hGS (Fig. 4d, red), consistent with the inhibition of hBest2-mediated currents by hGS when Cl^- was the principal anion in both sides of the patch solutions (Fig. 2). However, hGS did not affect hBest2-mediated currents when glutamate was the principal anion in the internal solution, regardless of whether Cl^- or glutamate was in the external solution (Fig. 4a, b, red). These results suggest that the inhibitory effect of GS on Best2 strengthens the entry barrier for extracellular glutamate but can be relieved by the *trans* promotive effect of glutamate from the intracellular side (Fig. 4j). Moreover, the reversal potentials were not affected by hGS in either case (E_{rev} = 50.3 ± 4.6 mV in Fig. 4d, and E_{rev} = −19.1 ± 2.9 mV in Fig. 4b, and Extended Data Fig. 7), indicating non-involvement of hGS in hBest2's ion selectivity between Cl^- and glutamate under these conditions (Fig. 4c, e).

Interestingly, when anions in the internal solution consisted of ~10% (13 mM) glutamate and ~90% (137 mM) Cl^-, which represents a more physiological condition, the relative permeability of glutamate to Cl^- drastically increased from 0.09 in the absence of hGS to 0.5 in presence of hGS (E_{rev} = 46.4 ± 2.2 mV and 15 ± 1.8 mV, respectively in Fig. 4g, h and Extended Data Fig. 7b). As these values resemble those from Cl^- or glutamate as the principal anion in the internal solution, respectively (Fig. 4b–e), our results suggest that hGS sensitizes hBest2 to intracellular glutamate, such that hBest2 can be activated by a low cytosolic concentration of glutamate in order to expel it. Furthermore, when an R to E mutation was introduced at R299, the conserved glutamate binding site on hGS, the resultant R299E mutant exhibited a loss of GS enzyme activity and an intact interaction with hBest2 (Extended Data Fig. 2a and 6c), but could no longer affect the E_{rev} of hBest2 under the 13 mM glutamate condition (Fig. 4g, h and Extended Data Fig. 7b). This indicates that hGS-mediated sensitization of hBest2 to intracellular glutamate is dependent on the binding of glutamate to hGS, which would presumably increase the local concentration of glutamate in proximity to hBest2 (Fig. 4j).

Anions pass through GS central cavity

The central cavity of bGS is hydrophilic and hydrated, with a 4.3 Å radius at one of the tightest points formed by the Cα hydrogens of G12 (Extended Data Fig. 4a–d). It structurally elongates the ion conducting pathway of bBest2 but does not represent a

constriction for passing anions such as Cl^- and glutamate, which have a radius of 1.8 Å and 3.5 Å in the dehydrated form, respectively. To test whether the conducted anions need to pass through the GS central cavity, we substituted G12 with a bulky Ile, Met or Trp, or a negatively charged Asp, generating the G12I/G12M/G12W/G12D mutants on hGS.

These G12 mutants of hGS were individually co-transfected with hBest2 into HEK293 cells for whole-cell patch clamp with glutamate and Cl^- in the internal and external solution, respectively. Both outward (Cl^- influx) and inward (glutamate efflux) currents from cells co-expressing hBest2 and any of the hGS mutants were significantly smaller than those from cells co-expressing hBest2 and WT hGS (Fig. 4i and Extended Data Fig. 5b and 8c), indicating a blockage of anion currents by the narrowed or negatively charged GS central cavity. Therefore, we concluded that the central cavity of GS is part of the ion passageway in the Best2-GS complex.

Involvement of the neck and aperture

As the *trans* promotion by intracellular glutamate and the inhibition by GS on Best2 both suggest the involvement of channel gating, we next sought to investigate the structural components in Best2 underlying these features. The neck and aperture are primary suspects, as they structurally constitute the two major restrictions in the ion conducting pathway of Best2 (Extended Data Fig. 4a, b), and are functionally critical for both channel gating and ion selectivity[11,23,24,32]. We previously reported a triple alanine substitution mutant at the neck, I76A/F80A/F84A (3A), and a single alanine substitution mutant at the aperture, K208A, which mimic constantly opened neck and aperture of Best2, respectively[11]. These mutants allow us to evaluate the contributions of the neck and aperture separately.

When the principal anion was glutamate and Cl^- in the internal and external solution, respectively, both inward and outward currents from the 3A and K208A mutants were only slightly elevated compared to those obtained when the principal anion was Cl^- on both sides, in sharp contrast to the significantly increased currents from WT hBest2 (Fig. 5a–c and Extended Data Fig. 5a, b). These results indicate that the glutamate-mediated *trans* promotive effect is impaired in both mutants, thus strongly suggesting the opening of both the neck and aperture by intracellular glutamate (Fig. 4j).

When the principal anion was Cl^- and glutamate in the internal and external solution, respectively, the presence of hGS decreased currents from the 3A mutant in a similar manner as observed with WT hBest2 (Fig. 4d, 5d and Extended Data Fig. 5c), but had no effect on the K208A mutant (Fig. 5e and Extended Data Fig. 5c), suggesting that hGS inhibits hBest2 via the aperture but not the neck. Moreover, the relative permeability of glutamate to Cl^- was significantly higher in both 3A and K208A mutants compared to WT hBest2 (Fig. 5d–f and Extended Data Fig. 7), consistent with our previous finding that both the neck and aperture contribute to ion selectivity of the channel[11,24,32].

Taken together, we concluded that both the neck and aperture play a critical role in the directional permeability of Best2 to glutamate, while the inhibitory effect of GS on Best2 is mediated through channel gating at the aperture.

Best2 and GS in NPE cells

To evaluate the influence of GS on Best2 under physiological conditions, we first investigated the role of hBest2 as a Ca^{2+}-activated Cl^- channel in human NPE cells, which has been suggested for years but never directly demonstrated. Robust Ca^{2+}-dependent Cl^- currents were recorded in human NPE cells by patch clamp with Cl^- as the principal anion in both internal and external solutions (Fig. 6a, b), and were significantly reduced by siRNA-mediated knockdown of endogenous hBest2 (Fig. 6b and Extended Data Fig. 2e and 9), demonstrating an essential role of hBest2 in conducting Ca^{2+}-dependent Cl^- currents in NPE.

When glutamate and Cl^- were the principal anion in the internal and external solution, respectively, both inward (glutamate efflux) and outward (Cl^- influx) currents were robust and significantly reduced by hBest2 knockdown (Fig. 6c), confirming the high permeability of hBest2 to intracellular glutamate in NPE cells. In sharp contrast, when glutamate and Cl^- were the principal anion in the external and internal solution, respectively, small outward (glutamate influx) currents were measured, along with an obvious shift of reversal potential (Fig. 6d), recapitulating the directional permeability to glutamate observed with transiently expressed hBest2 in HEK293 cells. Remarkably, these currents were significantly increased by siRNA-mediated knockdown of endogenous hGS (Fig. 6d and Extended Data Fig. 9). Moreover, when detected by immunostaining, the endogenous hBest2 and hGS showed enrichment and co-localization on the plasma membrane of human NPE cells (Fig. 6a *inset*). Taken together, our results strongly suggest a physiological role of hBest2 in releasing intracellular glutamate and the functional influence of hGS on hBest2 in NPE cells.

Discussion

Here, we report a directional permeability of Best2 to glutamate heavily biased towards efflux of intracellular glutamate. Based on the *trans* promotive effect of intracellular glutamate on Best2 and the gradually increased P_{Glu}/P_{Cl} under ascending concentrations of intracellular glutamate (Fig. 4f and Extended Data Fig. 8b), we propose a two-step process where intracellular glutamate (EC_{50} = 46 mM) first binds to Best2 for activating/opening of the channel, and then can be conducted. In this model, Best2 by itself has a very low permeability to the big anion glutamate when it is present on the extracellular side (Fig. 4d, e), but the occupancy of glutamate at putative intracellular binding site(s) causes the opening of both the neck and aperture of the channel, leading to a significantly increased glutamate conductivity (Fig. 4a, b, j). Meanwhile, as the neck and aperture are both critical for ion selectivity (Fig. 5f)[11,24], this intracellular glutamate-induced opening also results in an increase of glutamate selectivity (Fig. 4c and Extended Data Fig. 8b). In accord with this notion, the crystal structure of cBest1 illustrates three conserved Cl^-/anion binding sites on the channel periphery, including one located inside the cytosolic vestibule[22]. Moreover, conserved residues have been identified as putative anion binding sites in the bBest2 ion conducting pathway at both extracellular and cytosolic entrances of the channel[11]. We have attempted to solve the open-state bBest2 structure in the presence of glutamate, but so far are only able to obtain a structure with 25 mM glutamate at the highest concentration in the cryo-EM sample buffer, and the structure is still in the closed state unbound with glutamate.

Nevertheless, obtaining the glutamate-bound structure of Best2 will provide a clear picture of this mechanism.

A stable Best2-GS complex is identified from the ciliary body with at least three functional consequences: 1) Best2 tethers a fraction of GS to the membrane, causing a decrease of cytosolic GS activity; 2) GS inhibits the channel activity of Best2 in the absence of intracellular glutamate; 3) GS sensitizes Best2 to intracellular glutamate, which promotes the opening of Best2 to expel glutamate out of the cell. To our knowledge, these findings represent the first documentation of a direct interplay between an ion channel and an amino acid metabolic enzyme. Since Best2 is capable of conducting both Cl^- and glutamate, we speculate two non-exclusive roles of the Best2-GS complex *in vivo*: 1) it regulates IOP through a negative feedback loop, where ocular hypertension stimulates GS expression to inhibit Best2-mediated Cl^- conductance in NPE, ultimately resulting in reduced IOP; 2) it contributes to glutamate cytotoxicity, which can be induced upon ocular hypertension and represents a major threat to retinal neurons, by releasing glutamate from NPE.

The unaltered GS activity with or without Best2 measured using purified proteins and whole-cell lysate strongly suggests that the tethering of GS by Best2 to the cell membrane does not affect the catalytic activity of GS or the interaction between GS and its substrate glutamate. Moreover, Best2 is activated by a low concentration of intracellular glutamate in the presence of WT GS but not the glutamate-binding deficient R299E mutant, suggesting that GS sensitizes Best2 by increasing the local concentration of intracellular glutamate. Interestingly, hBest2 also exhibits a directional permeability for intracellular glutamine, in a similar manner as for glutamate (Extended Data Fig. 8d–f). Although it remains unclear whether glutamate concentrated by GS is directly expelled by Best2 or after conversion to glutamine, the Best2-GS complex represents a cooperative machinery to reduce intracellular glutamate level.

Our patch clamp data suggest that GS inhibits Best2 by affecting gating at the aperture (Fig. 5d, e), which is consistent with the binding of GS to the cytosolic side of Best2 in close proximity to the aperture (Fig. 1c and 4j). The binding of intracellular glutamate to Best2 likely opens both the neck and aperture, and thus overcomes the inhibitory effect of GS on the aperture. A potential alternative explanation is that the binding of intracellular glutamate leads to the dissociation of the Best2-GS complex. However, two results strongly argue against this idea: 1) the co-immunoprecipitation of Best2 and GS was not affected by the presence of glutamate (Extended Data Fig. 2a); 2) all the central cavity occluding mutants on G12 of GS caused a significant decrease of Best2-mediated currents compared to the WT GS when glutamate is in the internal solution, suggesting that these GS mutants are still bound to Best2 to block the currents in the presence of intracellular glutamate. Notably, all four critical residues mediating the Best2-GS interaction (R197 and D327 of Best2, and G23 and K52 of GS) are highly conserved among Best2 and GS orthologs across species, but neither R197 nor D327 is conserved in Best1 (L197 and Q327 in hBest1), suggesting paralog specificity of the Best2-GS interaction.

Methods

Pull-down of Best2 Interacting Complex from Ciliary Lysate

bBest2$_{1–406}$, which contains the first 406 amino acids of bBest2 and functionally resembles the full-length protein, was purified as previously described but without size exclusion chromatography[11,35]. The protein was bound to Ni-NTA resin by end-over-end rotation for 20–30 min and washed in 5–10 column volumes of buffer containing (in mM): 50 HEPES pH 7.8, 300 NaCl, 40 Imidazole, 5 $MgCl_2$, 5% (v/v) glycerol, 0.05% (w/v) n-dodecyl β-d-maltopyranoside (DDM) and then another 5–10 column volumes of buffer containing (in mM): 25 HEPES pH 7.8, 500 NaCl, 75 Imidazole, 5% (v/v) glycerol, 0.05% (w/v) DDM.

Ciliary bodies were harvested by dissecting bovine eyeballs and frozen in −80 °C until used. On the day of protein purification, 3 eyes' worth of ciliary body tissue (approximately 5–10 g) was thawed at RT and pulverized using a mortar and pestle under liquid nitrogen. The resulting powdered ciliary body tissue was resuspended in the same resuspension buffer as bBest2 and homogenized by a motor-driven tissue grinder. The resultant homogenate was lysed by sonication and incubated in 1% (w/v) sol-grade DDM for 1 h with vigorous rotation. The ciliary lysate was centrifuged at 35,000 rpm for 45 min in Beckman XL-90 ultracentrifuge with a Ti-45 rotor at 4 °C to pellet non-soluble material. The resultant ciliary lysate supernatant and bBest2-bound Ni-NTA resin were incubated with end-to-end rotation overnight at 4 °C. As a control for non-specific binding, empty Ni-NTA resin was incubated with ciliary body lysate at the same volume-volume ratio and treated in parallel.

On day 2, the pull-down resin was washed with the same buffers and procedures as on Day 1, and subjected to elution with one volume of elution buffer equivalent to the volume of solid Ni-NTA resin. The elution buffer contained (in mM): 25 HEPES, 200 NaCl, 5% (v/v) glycerol, 500 Imidazole, 0.05% (w/v) DDM. The eluted samples were sent for mass spectrometry.

Mass Spectrometry

Pull-down samples from bovine ciliary body lysate were subjected to in-solution digestion with LysC and trypsin followed by liquid chromatography with tandem mass spectrometry (LC-MS/MS) at the Proteomics and Macromolecular Crystallography Shared Resource of Columbia University. Samples were resuspended in 40 μL of freshly prepared sodium deoxycholate (SDC) lysis buffer (1% SDC, 10 mM TCEP, 40 mM CAA and 100 mM TrisHCl pH 8.5) and boiled at 60 °C for 20 min to denature and reduce and alkylate cysteines, followed by sonication in a water bath, cooled down to room temperature. Proteins were precipitated with acetone-salt method and pellets were resuspended in SDC lysis buffer (1% SDC and 100 mM TrisHCl pH 8.5). Protein digestion was processed overnight by adding LysC and trypsin in a 1:50 ratio (μg of enzyme to μg of protein) at 37 °C and 1,400 rpm. Peptides were acidified by adding 1% TFA, vortexed, and subjected to StageTip clean-up via SDB-RPS. Samples were dried in a SpeedVac and resuspended in 10 μL of LC buffer (3% ACN/0.1% FA). Peptide concentrations were determined using NanoDrop and 200 ng of each sample were used for PASEF analysis on timsTOF Pro.

Peptides were separated within 90 min at a flow rate of 400 nL/min on a reversed-phase C18 column with an integrated CaptiveSpray Emitter (25 cm x 75 μm, 1.6 μm, IonOpticks). Mobile phases A and B were with 0.1% formic acid in water and 0.1% formic acid in ACN. The fraction of B was linearly increased from 2 to 25% within 60 min, followed by an increase to 35% within 10 min and a further increase to 80% before re-equilibration.

The timsTOF Pro was operated in PASEF mode 2 with the following settings: Mass Range 100 to 1,700 m/z, 1/K0 Start 0.6 V·s/cm^2, End 1.6 V·s/cm^2, Ramp time 100 ms, Lock Duty Cycle to 100%, Capillary Voltage 1,600 V, Dry Gas 3 L/min, Dry Temp 200 °C, PASEF settings: 10 MSMS Frames (1.16 s duty cycle), charge range 0–5, active exclusion for 0.4 min, Target intensity 20,000, Intensity threshold 2,500, CID collision energy 59 eV. A polygon filter was applied to the *m/z* and ion mobility plane to select features most likely representing peptide precursors rather than singly charged background ions.

The acquired PASEF raw files were analyzed using the MaxQuant environment v.1.6.17.0 and Andromeda for database searches. The default is used for first search tolerance and main search tolerance (20 ppm and 6 ppm, respectively). MaxQuant was set up to search with the reference bovine proteome database downloaded from UniProt. MaxQuant performed the search trypsin digestion with up to 2 missed cleavages. Peptide, site and protein false discovery rates (FDR) were all set to 1%.

Cell Lines

HEK293 and HEK293F cells were purchased from ATCC (CRL-1573) and Thermo Fisher Scientific (R79007), respectively. As HEK293 is on the International Cell Line Authentication Committee's list of commonly misidentified cell lines, the cells used in this study were authenticated by short tandem repeat (STR) DNA profiling and tested negative for mycoplasma contamination. The culture medium was DMEM (4.5 g/L glucose, Corning 10013CV) supplemented with 100 μg/mL penicillin-streptomycin and 10% fetal bovine serum. Human NPE cells were purchased from ScienCell Research Laboratories (Cat. #6580), cultured in Epithelial Cell Medium (EpiCM, Cat. #4101) and authenticated by morphology. No mycoplasma contamination was found by DAPI staining.

Transfection

20–24 h before transfection, cells were split into new 3.5 cm culture dishes at 50% confluency. Plasmid and siRNA transfections were conducted using the PolyJet Transfection Reagent (SignaGen SL100688) and Lipofectamine RNAiMAX Reagent (Invitrogen 13778–030), respectively. The transfection mix was removed after 4–8 h, and cells were washed with PBS and fed with fresh media until downstream analysis or harvest.

Immunoblotting

The M-PER Mammalian Protein Extraction Reagent (Thermo Fisher Scientific 78501) and Mem-PER Plus Membrane Protein Extraction Kit (Thermo Fisher Scientific 89842) were used to prepare the whole-cell lysate and membrane fraction, respectively. After denaturing at 95 °C for 5 min, the samples were run on 4–15% gradient SDS-PAGE gel at room temperature, and wet transferred onto nitrocellulose membrane at 4 °C. The membranes

were incubated in blocking buffer containing 5% (w/v) non-fat milk for 1 h at room temperature, and subsequently incubated overnight at 4 °C in blocking buffer supplemented with primary antibody. Primary antibodies against the following proteins were used: GFP (1:1,000, Thermo Fisher Scientific, A-6455), GS (1:1,000, Sigma-Aldrich, HPA007316) and β-Actin (1:1,000, Thermo Fisher Scientific MA5–15739). IRDye® 680RD Goat anti-Mouse IgG (LI-COR, 926–68070) and IRDye® 800CW Donkey anti-Rabbit IgG (LI-COR, 925–32213) were used at a concentration of 1:10,000 and an incubation time of 1 h at room temperature, followed by infrared imaging on a Bio-Rad ChemiDoc system.

Immunoprecipitation

HEK293 cells were harvested 48 h post transfection by centrifugation at 1,000 x g for 5 min at room temperature. Cell pellets were lysed in pre-cooled lysis buffer (150 mM NaCl, 50 mM Tris, 0.5% IGEPAL® CA-630, pH 7.4) supplemented with protease inhibitor cocktails (Roche, 04693159001) for 30 min on ice, and then centrifuged at 13,000 rpm for 12 min at 4 °C. The supernatant (300 μg) was collected and mixed with 2 μg Myc monoclonal antibody (Thermo Fisher Scientific, MA1–21316). After rotating overnight at 4°C, the mixture was incubated with Dynabeads M-280 sheep anti-mouse IgG (Thermo Fisher Scientific, 11202D) for 5 h at 4 °C. After thorough washing of the beads, bound fractions were eluted in 1x SDS sample buffer (Bio-Rad, 1610747) by heating for 10 min at 75 °C. Co-immunoprecipitation samples and 1/10 of input (30 μg) were then resolved by SDS-PAGE and analyzed by immunoblotting.

Electrophysiology

Whole-cell patch clamp recording was conducted 48–96 h after splitting of NPE cells or transfection of HEK293 cells with EPC7 and EPC10 patch clamp amplifier (HEKA Electronics) controlled by Patchmaster v2×90.5 (HEKA)[36,37]. Micropipettes were pulled and fashioned from filamented 1.5 mm thin-walled glass (WPI Instruments). Series resistance was typically 1.5–2.5 MΩ, with no electronic series resistance compensation. Experiments were conducted at room temperature (23 ± 2 °C). Liquid junction potentials were measured and corrected using HEKA built-in functions. The standard zero Ca^{2+} pipette solution contained (mM): 146 CsCl, 2 $MgCl_2$, 5 EGTA, 2 MgATP (added fresh), 10 HEPES, pH 7.3 adjusted with NMDG. Solutions with various free Ca^{2+} concentrations were made by mixing $CaCl_2$ with EGTA as calculated by the MaxChelator Program, and the free Ca^{2+} concentration was verified using a Ca^{2+} ion-selective electrode. The standard extracellular solution contained (mM): 140 NaCl, 5 KCl, 2 $CaCl_2$, 1 $MgCl_2$, 15 glucose, 10 HEPES, pH 7.4 with NMDG. In glutamate containing solutions, 140 mM Na-glutamate replaced NaCl in the external solution, and 146, 113, 80, 46, or 13 mM Cs-glutamate replaced CsCl in the internal solution, pH 7.4 adjusted with NMDG. In glutamine containing solutions, 140 mM glutamine replaced NaCl in the external solution, and 146 mM glutamine replaced CsCl in the internal solution, pH 7.4 adjusted with NMDG. Solution osmolarity was 290~310 mOsm/L with glucose, and ~5 mOsm lower in the internal solutions than the external solutions of the same experiment. The low and high Ca^{2+} solutions in the same set of experiments were adjusted to have the exact same osmolarity. Solution changes were performed manually.

Electrophysiological Data Collection and Analyses

Traces were acquired at a repetition interval of 4 s[28]. Currents were sampled at 25 kHz and filtered at 5 or 10 kHz. I-V curves were generated from a group of step potentials (−100 to +100 mV from a holding potential of 0 mV). Data were processed off-line in Patchmaster. Statistical analyses were performed using built-in functions in OriginPro 8.5. Relative permeability was calculated according to the Goldman-Hodgkin-Katz equation. The relative Glu/Cl^- (with glutamate or Cl^- in the internal solution) outward movement (inward current) conductance ($G_{Glu\ with\ in\text{-}Glu}$ /$G_{Cl\ with\ in\text{-}Cl}$) was measured as slope conductance at the reversal potential minus 50 mV. The *trans* effect, representing the relative Cl^- (in the external solution) inward movement (outward current) conductance ($G_{Cl\ with\ in\text{-}Glu}$/$G_{Cl\ with\ in\text{-}Cl}$) was measured as slope conductance at the reversal potential plus 50 mV. The relative Glu/Cl^- (with glutamate or Cl^- in the external solution) inward movement (outward current) conductance ($G_{Glu\ with\ ex\text{-}Glu}$ /$G_{Cl\ with\ ex\text{-}Cl}$) was measured as slope conductance at the reversal potential plus 50 mV. The relative Cl^- (in the internal solution) outward movement (inward current) conductance ($G_{Cl\ with\ ex\text{-}Glu}$/$G_{Cl\ with\ ex\text{-}Cl}$) was measured as slope conductance at the reversal potential minus 50 mV. The “n” value in patch clamp recording figure legends indicates the total number of individual cells.

Molecular Cloning

All constructs were made by site-directed mutagenesis PCR with the In-fusion Cloning Kit (Clontech) and verified by sequencing.

Immunofluorescence

NPE cells cultured on coverslips were washed with PBS twice, and fixed in 4% sucrose and 4% paraformaldehyde at room temperature for 45 min. The fixed cells were permeabilized in PBS containing 0.25% Triton X-100 at room temperature for 10 min. To block non-specific binding sites, the samples were incubated with PBS containing 5% BSA at room temperature for 1 h. Primary antibodies were diluted in blocking solution as follows: rabbit anti-Best2 (Sigma-Aldrich, HPA046229), 1:1000; mouse anti-GS (Thermo Fisher Scientific, MA5–27749), 1:500. The samples were incubated with primary antibody in blocking solution overnight at 4 °C. The next day, the samples were washed with PBS thrice. Then, Alexa Fluor 647 conjugated donkey anti-rabbit IgG (Abcam, ab150075) and Alexa Fluor 488 conjugated goat anti-mouse IgG (Abcam, ab150113) were diluted 1:1000 in blocking solution and incubated with cells at room temperature for 1 h. Unbound secondary antibody was washed away with PBS thrice. After thorough washing, coverslips were mounted onto ProLong Diamond Antifade Mountant (Thermo Fisher Scientific, P36961). A Nikon A1 laser scanning confocal microscope was used to acquire images, which were then processed in Fiji (https://fiji.sc/).

FRET Two-hybrid Assay

HEK293 cells were cultured for 48–72 h after transfection. Protein synthesis inhibitor cycloheximide (100 μM) was added to cells 2 h prior to experimentation to halt synthesis of new fluorophores and allow existing fluorophores to fully mature, and cells were resuspended in PBS.

An LSR II (BD Biosciences) flow cytometer was utilized for FRET measurements. Forward and side scatter signals were detected and used to gate for single and healthy cells. For determining FRET efficiency, three distinct fluorescence signals were measured: 1) Cerulean emission through direct excitation measured through the BV421 channel (excitation, 405 nm; emission, 450/50); 2) Venus emission from direct excitation measured via the fluorescein isothiocyanate channel (excitation, 405 nm; dichroic, 505 LP; emission, 525/50); 3) Venus emission because of FRET via the BV510 channel (excitation, 405 nm; dichroic, 505 LP; emission, 525/50). Flow cytometric signals were collected at a medium flow rate (2,000 to 8,000 events/s). Fluorescence data were exported as Flow Cytometry Standard 3.0 files for further processing and analysis using custom MATLAB functions (MathWorks)[34]. For each FRET pairs, $K_{d,EFF}$ was obtained.

Cryo-EM Sample Preparation

bBest2 was produced and purified as previously described[11]. In brief, bBest2-GFP-His was expressed by the BacMam system in HEK293F suspension culture at 30 °C. Cells were collected on day 4, resuspended in buffer containing 300 mM NaCl, 50 mM HEPES, 20 mM imidazole, 5% (v/v) glycerol, 1 mM PMSF, EDTA-free protease inhibitor cocktail (Sigma S8830) and lysed by sonication on ice. Cellular debris was removed by low-speed centrifugation, and membranes were collected by ultracentrifugation of the supernatant. Membranes were extracted in 2% (w/v) DDM by slow rotation at 4 °C for 2 h. The insoluble fraction was removed by ultracentrifugation and supernatant containing the detergent-soluble fraction was passed over Ni^{2+}-NTA resin, washed with 10 column volumes of wash buffer containing up to 125 mM imidazole, and eluted in similar buffer containing 500 mM imidazole. Protein was exchanged to low imidazole buffer by multiple rounds of concentration and dilution in a 100 kDa centrifugal filter unit (Amicon Ultra-15, Millipore). Protein in ~ 50 mM imidazole was treated overnight with TEV protease to remove the GFP-His tag, and TEV and free GFP-His were removed by Ni^{2+} -NTA resin. Pure protein was transferred to amphipol PMAL-C8, treated with bio-beads overnight, and a final round of size exclusion chromatography was performed in the absence of detergent on a Superdex-200 increase 10/300 (GE Healthcare).

Strep-tagged bGS (Strep-bGS) was produced from a bacterial expression vector (pNYCOMPS-N23-Strep) in the BL21 *E. coli* strain. Cells were grown in TB media (Thermo Scientific K75856-A1) to OD_{600} 0.6–0.8 and bGS expression was induced by 0.4 mM IPTG. After overnight culture at 20 °C, cells were collected on ice and sonicated in resuspension buffer containing 200 mM NaCl and 50 mM HEPES, pH 7.8. The lysate was centrifuged to remove insoluble fraction and supernatant was incubated with Strep-Tactin resin, washed, and eluted in similar buffer containing 20 mM desthiobiotin. The eluted protein was concentrated and run on a Superdex200 increase 10/300 by HPLC (GE Healthcare). The final bGS protein product was concentrated to 0.7 mg/mL. Purified bBest2 and bGS were incubated at 1:2 molar ratio for 1 h on ice and then directly used to make grids on the Vitrobot as previously described[11].

Data Collection and Image Processing

Grids were clipped, screened, and then transferred to a Krios G3i equipped with K3 for data collection at Columbia's Cryo-EM Core Facility (Hammer Krios 1). 795 K3 movies were collected with Leginon 3.5, each containing 50 frames at a total dose of 58 $e^-/Å^2$ and a magnification corresponding to 0.83 $Å^2$/pix. Movies were aligned using MotionCorr2 within RELION-3.1[38]. Aligned micrographs were imported to cryoSPARCv3.1.0 for subsequent patch CTF estimation, particle picking, extraction, and initial cleanup by 2D classification. Particle picking was initially performed using bBest2 as the template, followed by extraction with large box size, revealing the complex. The bBest2-bGS-bBest2 "sandwich" was identified as the major class of interest and this particle was used for the final round of particle picking. 78,623 initial particles were extracted with binning to 4.98 $Å^2$/pix and subjected to one round of 2D classification. 25,618 particles corresponding to the bBest2-bGS-bBest2 sandwich were re-extracted without binning and subjected to *Ab initio* reconstruction and homogeneous refinement. Refined maps exhibited D5 symmetry; thus, homogeneous refinement was repeated with D5 symmetry enforced with on-the-fly optimization of per-particle defocus and per-group CTF parameters, yielding a 2.14 Å map. Particles underwent one round of polishing in RELION-3.1[39], followed by a final round of non-uniform refinement to 2.0 Å[40]. A locally filtered map was generated in cryoSPARC and used for model building and refinement.

Model Refinement and Validation

The initial model for bBest2 was obtained from our previously published structure (PDB 6VX7) and the hGS crystal structure (PDB 2OJW) was used as template for SWISS-MODEL to generate the initial model for bGS[41]. Manual refinement was performed in coot 0.9.8.1[42], along with real space refinement in Phenix 1.19.2 and validation by comprehensive validation tools in Phenix[43], including MolProbity to assess geometry constraints[44], phenix.mtriage to compute the map-to-model FSC, and EMRinger 1.0.0 and MapQ 1.6.2 to assess model fit[45–47]. All figures depicting the model and/or map were made with Chimera v1.16.

siRNA Design

The sense strand sequences of gene-specific siRNAs are as following: hGS, GCUUGUAUGCUGGAGUCAA; hBest2, CAGUGGACGAGAUGUAUGA. The scramble control siRNA was purchased from Sigma-Aldrich (Cat. #SIC001)

qRT-PCR

Total RNA was extracted from cell pellets with the PureLink RNA Mini Kit (Thermo Fisher Scientific, 12183020) and subjected to cDNA synthesis using the RevertAid First Strand cDNA synthesis kit (Thermo Fisher Scientific, K1621). The resultant cDNA was used as the template for qPCR amplification with gene-specific primer sets: hBest2, GCGCTACTTCGAGAAGCTTGT and CGGGCAGCGGCAT; hGS, GGATCGATGGTACTGGAGAAGG and GCACGAGATACATGTCA CTGTTGG; β-Actin, CACCATTGGCAATGAGCGGTTC and AGGTCTTTGCGGATGTCCACGT.

Glutamine Synthetase Activity Assay

GS activity was measured by the BioVision Glutamine Synthetase Activity Assay Kit (BioVision K2056–100). For cell-based experiments, cell pellets were lysed in the provided GS Assay Buffer (for cytosolic GS activity) or the M-PER Mammalian Protein Extraction Reagent (for overall GS activity) and incubated on ice for 10 min, followed by centrifugation at 12,000 x g for 15 min at 4 °C. The supernatant was collected, measured by BCA assay to determined protein concentration, and then subjected to GS activity assay according to instructions from the kit. For protein-based experiments, purified bGS and bBest2 proteins were mixed at 1:1, 1:2, and 1:5 molar ratios, and incubated on ice for 60 min prior to GS activity assay. A SpectraMax M5 Microplate Reader was used for colorimetric measurements at 570 nM. The unit of GS activity is defined as U = nmol/min.

Statistics and Reproducibility

A sufficient number of samples were examined to reach statistical conclusion according to the specific method utilized in that experiment. Statistically significant differences ($p < 0.05$) between means of two groups were determined by two-tailed unpaired Student's t test. Data are presented as means values +/− SEM. Immunoblotting, FRET and GS activity experiments were biologically replicated three times with similar results.

Data and Materials Availability

The atomic model and cryo-EM reconstruction of the bBest2-bGS complex are deposited to the Protein Data Bank (8ECY, http://doi.org/10.2210/pdb8ecy/pdb) and Electron Microscopy Data Bank (EMD-28025, https://www.ebi.ac.uk/pdbe/entry/emdb/EMD-28025). All materials are available from the corresponding author upon request.

Extended Data

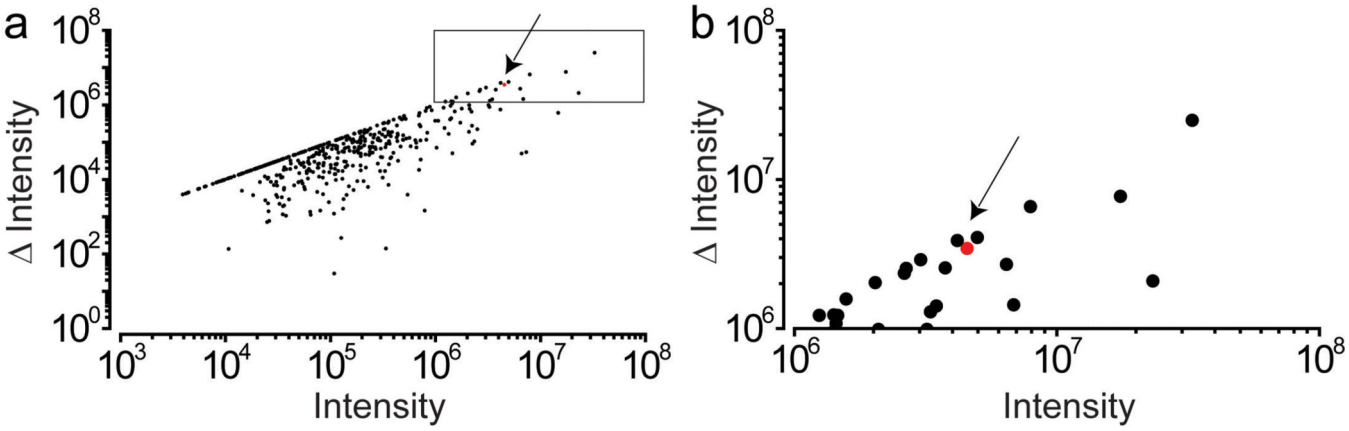

Extended Data Figure 1. Identification of bBest2-GS interaction by mass spectrometry.

(**a, b**) Dot plots showing the signal intensities of positive hits from mass spectrometry analysis with ciliary body lysate pull-down samples. X axis, signal intensity in the bBest2 pull-down sample; Y axis, change of signal intensity calculated by subtracting the signal intensity of the control pull-down sample (bovine ciliary lysate with empty Ni^+ beads) from

that of the bBest2 pull-down sample. The dot representing bGS is labeled red in the total (**a**) and high intensity (**b**) data sets.

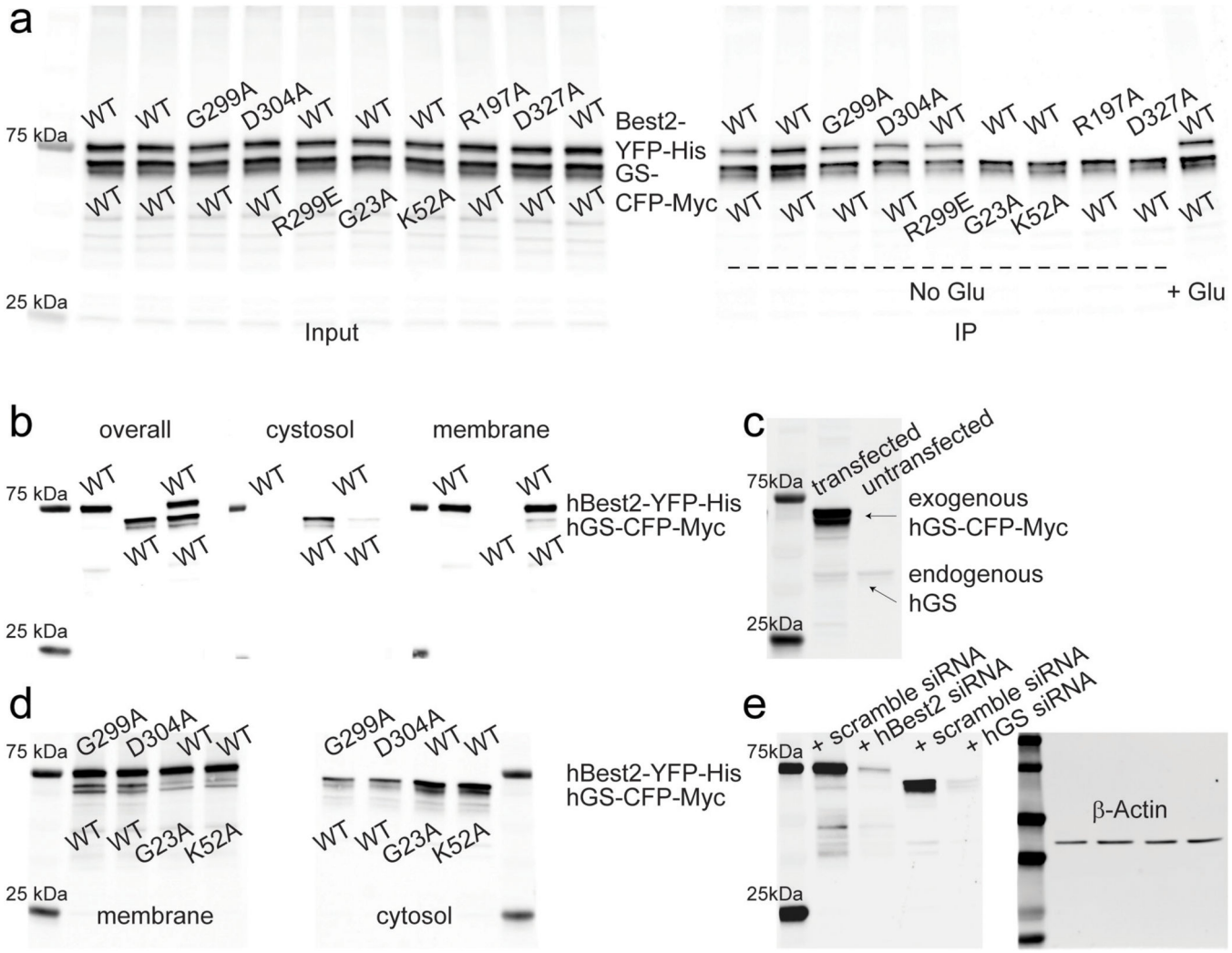

Extended Data Figure 2. Immunoblotting of Best2 and GS in HEK293 cells.

(**a**) Indicated Best2-YFP-His and GS-CFP-Myc constructs were co-expressed and detected by an anti-GFP antibody in input (*left*) and co-immunoprecipitation (*right*) samples. The last lane on the IP gel is performed in the presence of 20 mM glutamate. (**b**) The overall, cytosolic and membrane-bound protein levels of WT hBest2-YFP-His and hGS-CFP-Myc upon individual- or co-expression were detected by an anti-GFP antibody. (**c**) Exogenous hGS-CFP-Myc and endogenous hGS in HEK293 cells were detected by an anti-GS antibody. (**d**) The cytosolic and membrane-bound levels of indicated hBest2-YFP-His and hGS-CFP-Myc constructs upon co-expression were detected by an anti-GFP antibody. (**e**) hBest2-YFP-His and hGS-CFP-Myc were individually co-transfected with hBest2 siRNA and hGS siRNA, respectively, or a scramble siRNA, and detected with an anti-GFP antibody *(left*). β-Actin (*right*) served as the loading control on the same blot. Each experiment was biologically replicated three times with similar results.

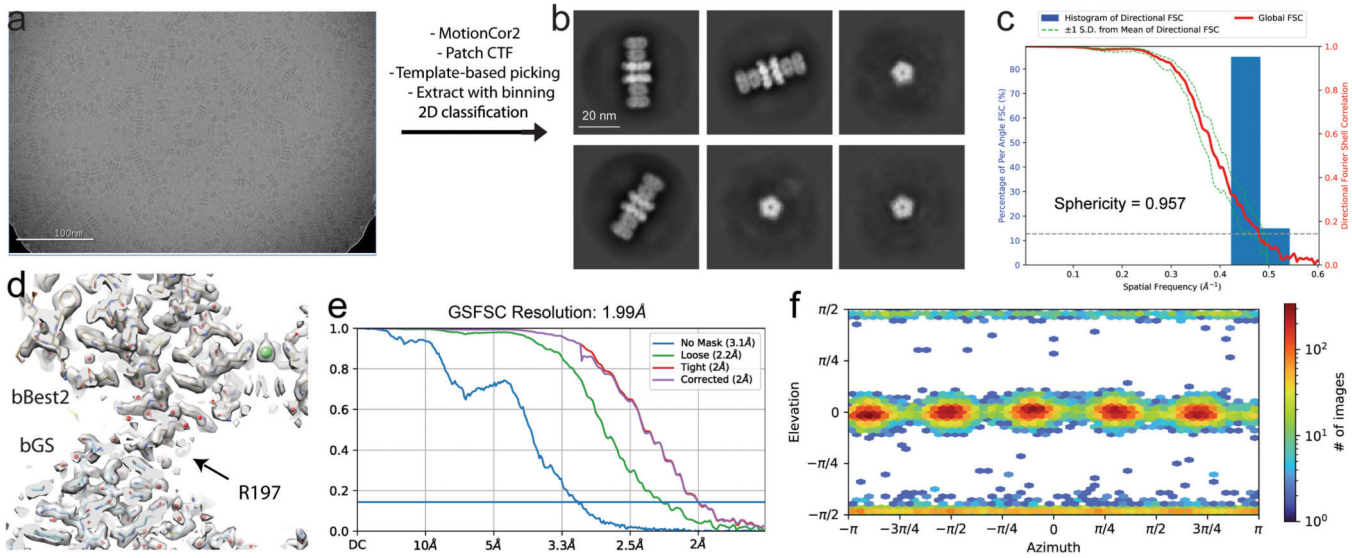

Extended Data Figure 3. Cryo-EM single-particle analysis processing workflow for obtaining the bBest2-GS co-structure.

(**a**) Representative motion-corrected micrograph. (**b**) Representative 2D class averages after selecting for the complex of interest. The bBest2-GS-Best2 sandwich is solved in cryo-EM with protein overexpression, while only one Best2 to GS is physiologically relevant, as Best2 is a membrane protein and GS is a cytosolic protein that forms polymers (including decamer) in solution in the absence of Best2. (**c**) The 3DFSC curve. (**d**) Density map and model for the co-structure viewed perpendicular to the binding interface, with bBest2 (tan) on top (R197 is labeled) and bGS (blue) on the bottom; local filtered map is shown at sigma 7.0. (**e**) FSC curve for final refinement with D5 symmetry imposed. (**f**) The viewing angle distribution.

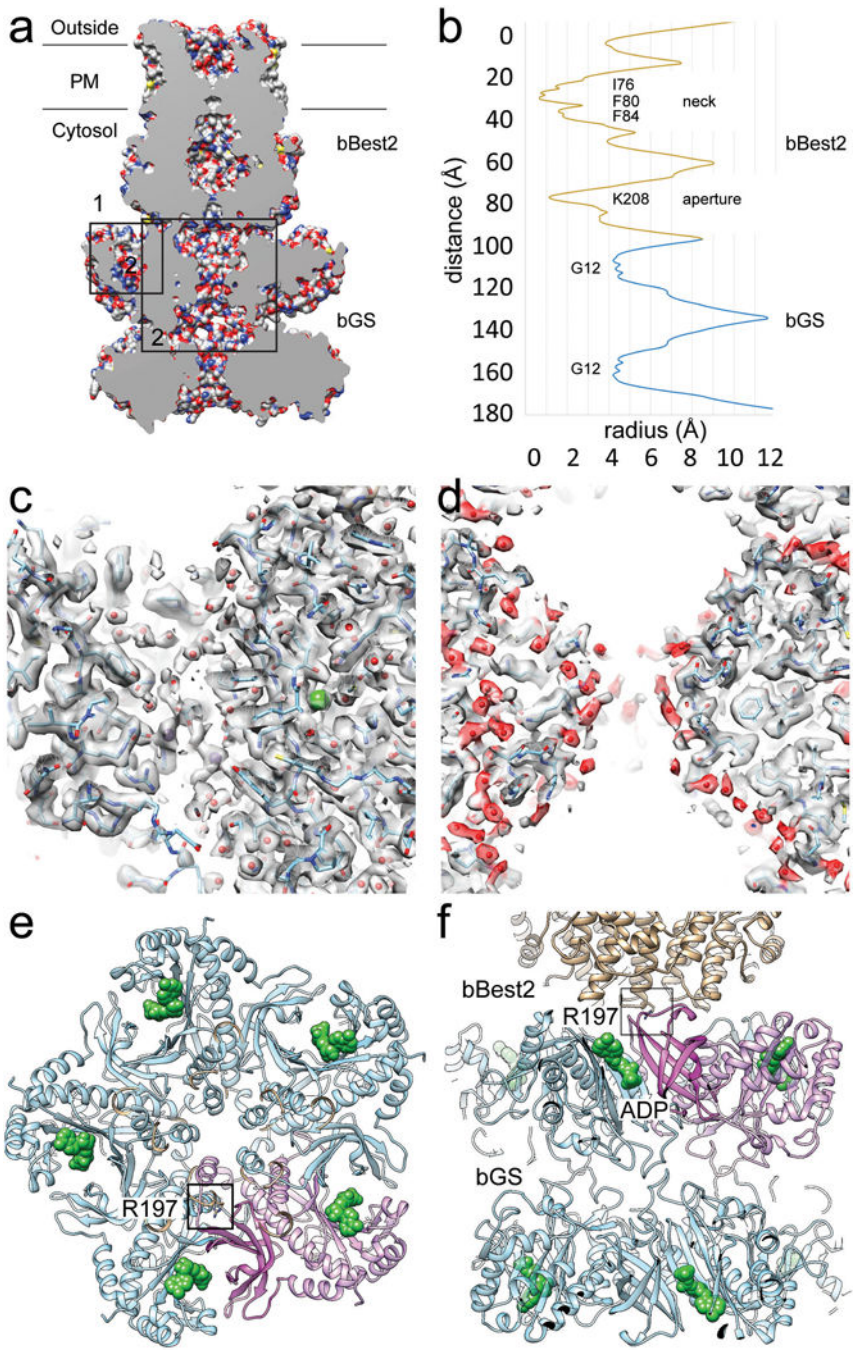

Extended Data Figure 4. The catalytic region of bGS is not affected by bBest2 binding.

(**a**) Inner view of the bBest2-GS ion-conducting pathway depicted as a surface and colored by element (N = blue, O = red, C = grey) demonstrating the hydrophilic surface. Box 1 represents the active and ATP-binding site, while box 2 represents the hydrophilic central cavity of bGS. (**b**) HOLE graph of the ion permeation pathway radius as a function of distance along the central axis of bBest2 and bGS. (**c**) Cryo-EM density corresponding to box 1 from panel **a** depicting the model for the ATP/ADP-free active site; local filtered map is shown at sigma 6.8. (**d**) Cryo-EM density corresponding to box 2 from panel

a depicting the hydrated hydrophilic central cavity with density corresponding to water molecules colored red; local filtered map is shown at sigma 6.8. (**e**) View from inside the bBest2 (tan) aperture looking away from the membrane towards bGS (blue). (**f**) Side view of the bGS active site with bBest2 sitting on top. The black box indicates R197 of bBest2 interacting with bGS. One protomer of bGS is colored pink with the beta grasp in dark pink. One molecule of ADP (green), taken from the original PDB 2OJW, is placed within the active site at the interface of two adjacent bGS protomers, illustrating the location of the active site in relation to the bBest2 binding site.

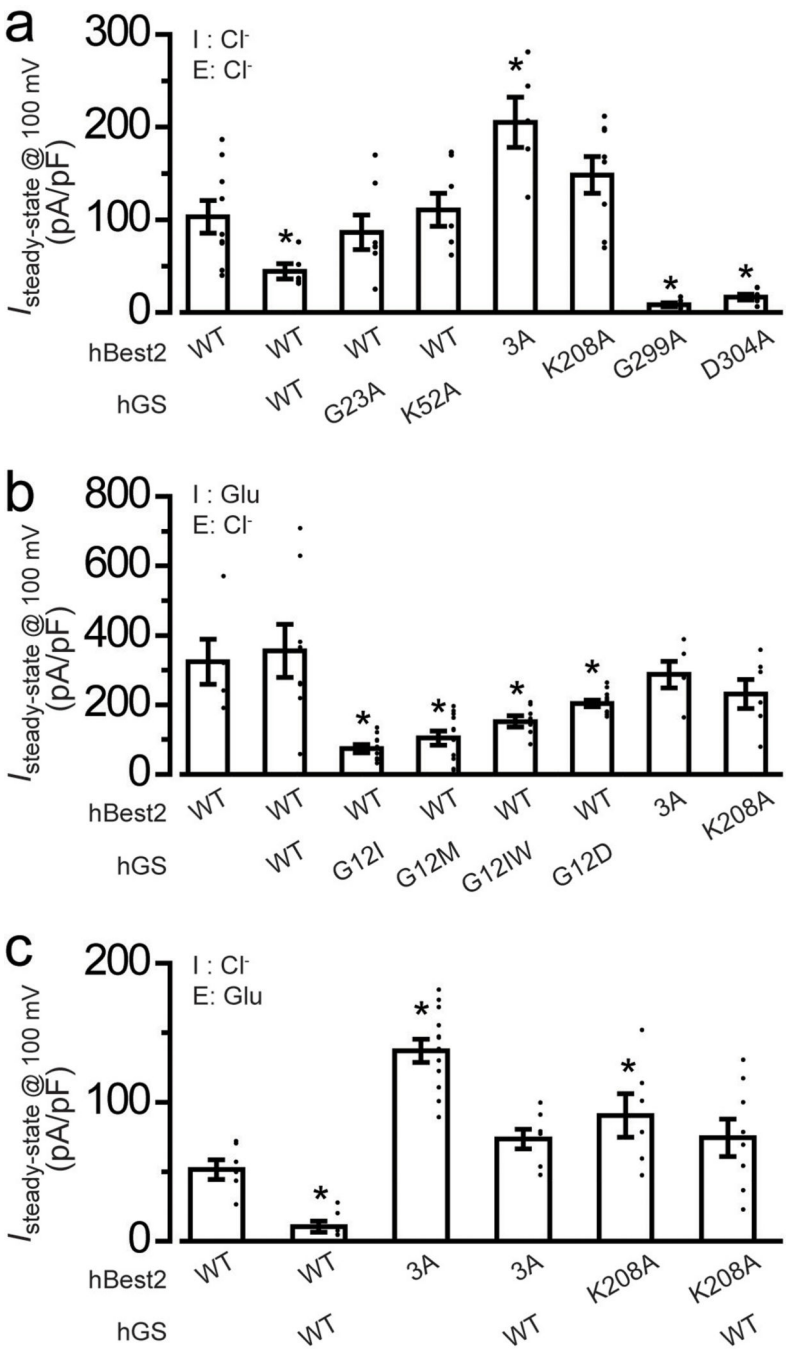

Extended Data Figure 5. Anion currents from hBest2 variants and the influence of hGS.

(**a-c**) Bar chart showing the steady-state current densities at +100 mV from HEK293 cells transiently expressing the indicated hBest2 and hGS constructs with 1 μM $[Ca^{2+}]_i$ under different conditions: (**a**) Cl^- as the principal internal and external anion; n = 9, 5, 7, 7, 5, 8, 5 and 6 for the groups from left to right, respectively; **p* = 0.04, 7E-3, 2E-3 and 2E-3 for the groups from left to right, respectively, compared to currents from cells expressing WT hBest2 alone. (**b**) Internal glutamate and external Cl^- as the principal anions; n = 5, 8, 9, 11, 7, 11, 5 and 6 for the groups from left to right, respectively; **p* = 3E-4, 9E-4, 0.01 and 0.02

for the groups from left to right, respectively, compared to currents from cells expressing WT hBest2 alone. (**c**) Internal Cl^- and external glutamate as the principal anions; n = 6, 6, 12, 7, 6 and 8 for the groups from left to right, respectively; *p = 5E-4, 6E-6 and 0.047 for the groups from left to right, respectively, compared to currents from cells expressing WT hBest2 alone. All error bars are presented as mean values +/− SEM; p values are calculated by two-tailed unpaired Student's t test.

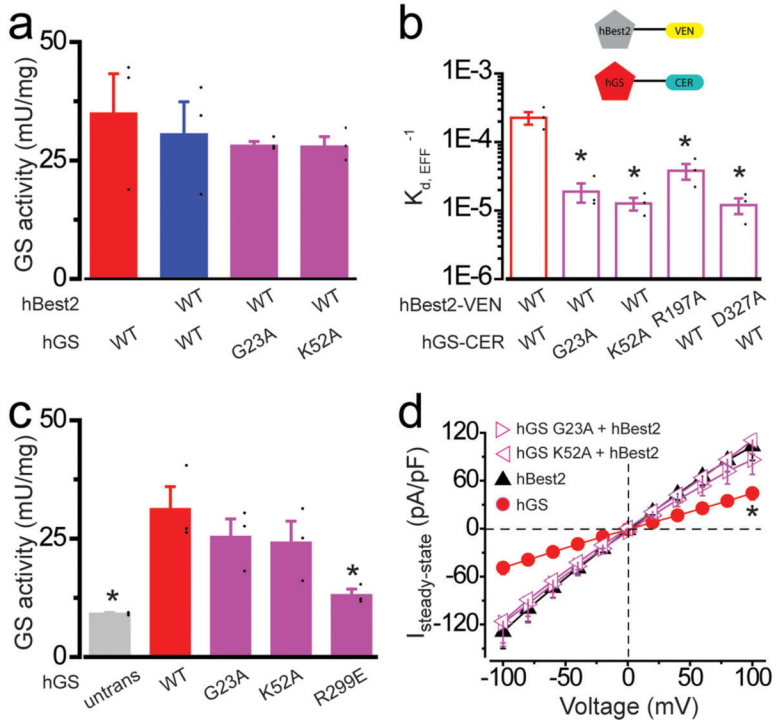

Extended Data Figure 6. Contributions of residues at the Best2-GS interacting interface.

(**a**) Bar chart showing GS activities in the whole-cell lysates of HEK293 cells transiently transfected with indicated hBest2 and hGS constructs; n = 3 for each group. (**b**) FRET two-hybrid analysis of the interaction between Cerulean-tagged hGS and Venus-tagged hBest2 constructs. Bar chart showing $1/K_{d,EFF}$ of the interaction; n = 3 for each group; *p = 0.01, 0.01, 0.02 and 0.01 for the WT-mutant pairs from left to right, respectively, compared to the WT-WT pair. (**c**) Bar chart showing GS activities in the cytosolic lysates of HEK293 cells transiently transfected with indicated hGS constructs; n = 3 for each group; *p = 9E-3 and 0.02 for untransfected and hGS R299E transfected cells, respectively, compared to cells transfected with WT hGS. (**d**) Population steady-state current density-voltage relationships of hBest2 in the presence of hGS G23A or K52A mutant (magenta triangles, n = 7 for each group), compared to hBest2 without (black triangle, n = 9) or with WT hGS (red circle, n = 5) at 1 μM $[Ca^{2+}]_i$ in transiently transfected HEK293 cells; *p =0.04 compared to currents from cells expressing hBest2 alone. All error bars are presented as mean values +/− SEM; p values are calculated by two-tailed unpaired Student's t test.

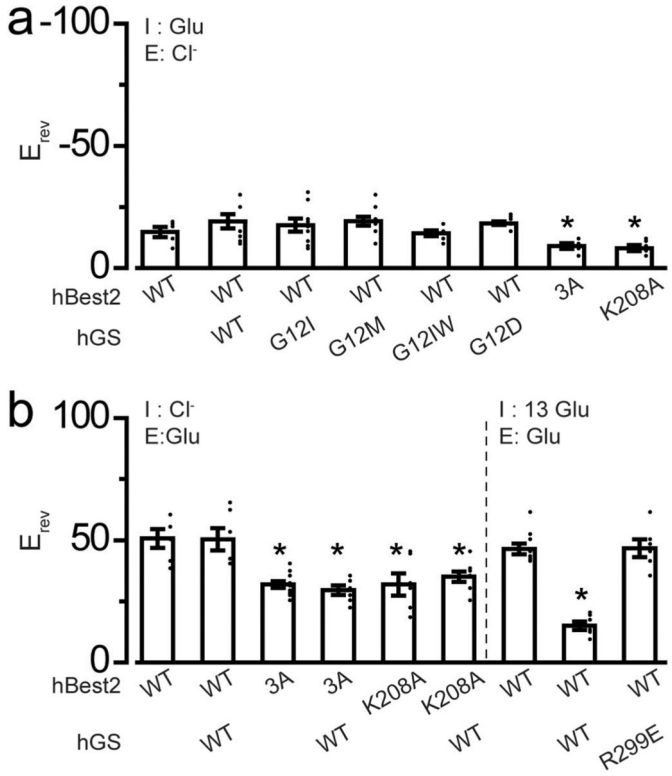

Extended Data Figure 7. Reversal potentials of hBest2 variants and the influence of hGS.

(**a**-**b**) Bar chart showing the reversal potentials from HEK293 cells transiently expressing the indicated hBest2 and hGS constructs at 1 μM $[Ca^{2+}]_i$ under different conditions: (**a**) Internal glutamate and external Cl^- as the principal anions; n = 5, 8, 9, 11, 7, 11, 5 and 6 for the groups from left to right, respectively; **p* = 0.04 and 0.02 for 3A and K208A, respectively, compared to currents from cells expressing WT hBest2 alone. (**b**) Internal Cl^- and external glutamate as the principal anions; n = 6, 6, 12, 7, 6, 8, 9, 6 and 6 for the groups from left to right, respectively. *p* = 3E-5, 3E-4, 0.01, 2E-3 and 2E-7 for the groups from left to right, respectively, compared to currents from cells expressing WT hBest2 alone. All error bars are presented as mean values +/− SEM; *p* values are calculated by two-tailed unpaired Student's *t* test.

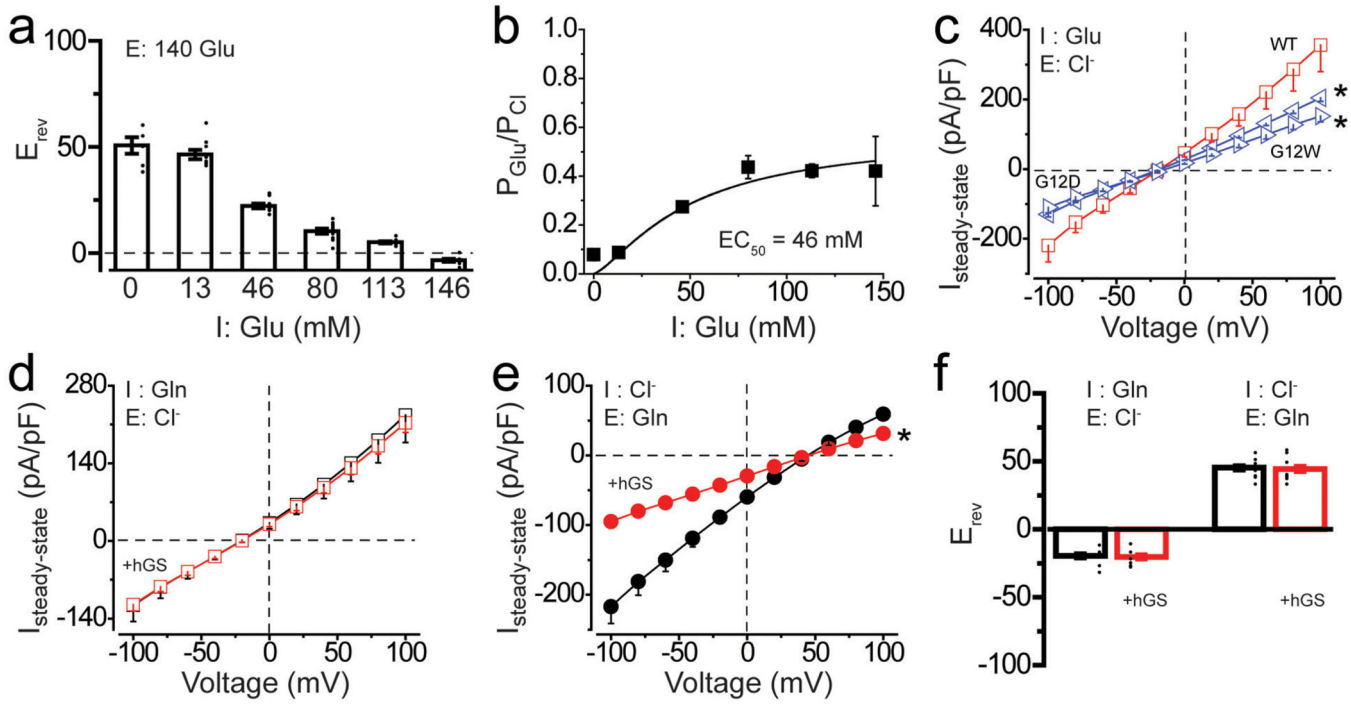

Extended Data Figure 8. Influence of hGS on the permeability of hBest2 to glutamate and glutamine.

(**a, b**) Reversal potentials (**a**) and relative ion permeability ratios of glutamate to Cl^- (**b**) from HEK293 cells transiently expressing hBest2 with 140 mM external glutamate and different concentrations of internal glutamate at 1 μM $[Ca^{2+}]_i$; n = 6, 9, 9, 11, 11 and 9 for the groups from left to right, respectively. (**c**) Population steady-state current density-voltage relationships in HEK293 cells transiently expressing hBest2 and WT (red, n = 8) or mutant (blue, n = 11 and 7 for G12D and G12W, respectively) hGS at 1 μM $[Ca^{2+}]_i$ with internal glutamate and external Cl^- as the principal anions; **p* = 0.03 for both G12D and G12W, compared to WT GS. (**d**) Population steady-state current density-voltage relationships in HEK293 cells transiently expressing hBest2 alone (black, n = 10) or hBest2 + hGS (red, n = 9) at 1 μM $[Ca^{2+}]_i$ with internal glutamine and external Cl^- as the principal anions. (**e**) The same format as **d**, but with external glutamine and internal Cl^- as the principal anions; n = 11 for each group; **p* = 7E-3 compared to hBest2 alone. (**f**) Reversal potentials calculated from **d, e**. All error bars are presented as mean values +/− SEM; *p* values are calculated by two-tailed unpaired Student's *t* test.

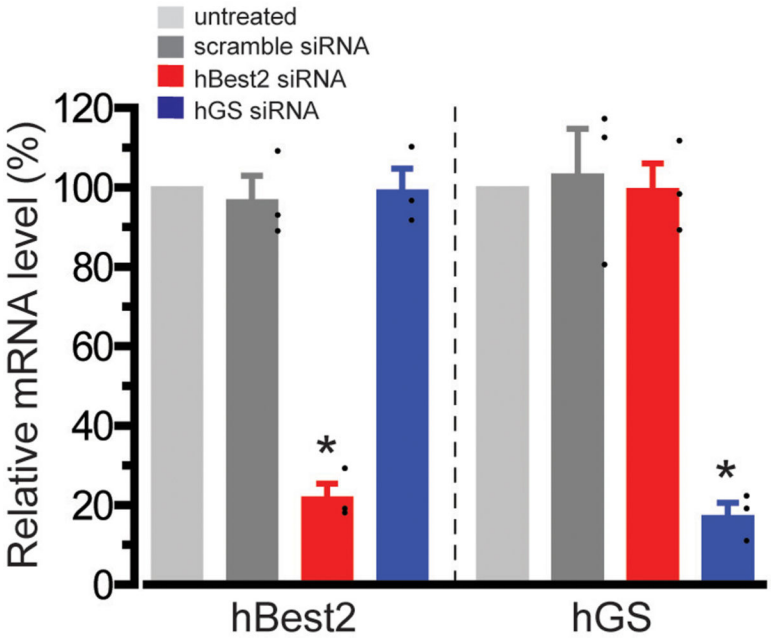

Extended Data Figure 9. Knockdown of hBest2 and hGS in human NPE cells.

The relative mRNA levels of hBest2 and hGS in cells treated with a scramble, hBest2-specific or hGS-specific siRNA were analyzed by qRT-PCR and normalized to those in untreated cells; n = 3 for each group; *p = 5E-4 and 2E-3 for hBest2 and hGS mRNA levels in cells treated with hBest2- and hGS-specific siRNA, respectively, compared to those in cells treated with the scramble siRNA by two-tailed unpaired Student's t test. All error bars are presented as mean values +/− SEM.

Extended Data Table 1.

Cryo-EM data collection, refinement and validation statistics.

	bBest2-bGS complex (EMDB-28025) (PDB 8ECY)
Data collection and processing	
Magnification	105,000
Voltage (kV)	300
Electron exposure (e-/A^2)	58
Defocus range (μm)	1.0–2.0
Pixel size (A)	0.83
Symmetry imposed	D5
Initial particle images (no.)	78,623
Final particle images (no.)	25,618
Map resolution (A)	1.99
FSC threshold	0.143
Map resolution range (A)	1.9–7.0
Refinement	
Initial model used (PDB code)	6VX7 (for bBest2)

	bBest2-bGS complex (EMDB-28025) (PDB 8ECY)
	20JW (for bGS)
Model resolution (A)	2.1
FSC threshold	0.5
Model resolution range (A)	2.0–7.0
Map sharpening *B* factor (A^2)	N/A (local resolution-filtered sharpening)
Model composition	
Non-hydrogen atoms	46,485
Protein residues	5,540
Ligands	MN: 20
	CA: 5
	CL: 11
	Water: 2,024
B factors (A^2)	
Protein	53.92
Ligand	45.42
R.m.s. deviations	
Bond lengths (A)	0.012
Bond angles (°)	1.319
Validation	
MolProbity score	1.48
Clashscore	8.48
Poor rotamers (%)	0
Ramachandran plot	
Favored (%)	97.91
Allowed (%)	2.09
Disallowed (%)	0

Acknowledgments

We thank Wayne Hendrickson and Criss Hartzell for comments on the paper, Allen Hsu for helping purify bGS, Yang Kong for helping set up qRT-PCR, Manu Ben-John and Pedro J. del Rivero Morfin for helping set up FRET, Rajesh Soni at the Proteomics and Macromolecular Crystallography Shared Resource of Columbia University for helping with mass spectrometry analysis, Renato Bruni at Center on Membrane Protein Production and Analysis (COMPPÅ) for providing the bacterial expression vector, and the Unrestricted Grant from Research to Prevent Blindness (RPB) to the Department of Ophthalmology at Columbia University. Cryo-EM data were collected within the Columbia Cryo-EM Core. A.P.O. was supported by NIH grants R01GM107462 and F31EY030763, K.Y. was supported by NIH grants R01EY014852 and R01GM132598, and T.Y. was supported by NIH grants R01GM127652 and R24EY028758, the Irma T. Hirschl/Monique Weill-Caulier Research Award (CU20-4313) and Schaefer Research Award.

References

1. Bakall B. et al. Bestrophin-2 is involved in the generation of intraocular pressure. Investigative ophthalmology & visual science 49, 1563–1570, doi:49/4/1563 [pii]10.1167/iovs.07-1338 (2008). [PubMed: 18385076]

2. Owji AP, Kittredge A, Zhang Y. & Yang T. Structure and Function of the Bestrophin family of calcium-activated chloride channels. Channels (Austin) 15, 604–623, doi:10.1080/19336950.2021.1981625 (2021). [PubMed: 34612806]
3. Zhang Y. et al. Enhanced inflow and outflow rates despite lower IOP in bestrophin-2-deficient mice. Investigative ophthalmology & visual science 50, 765–770, doi:iovs.08–2501 (2009). [PubMed: 18936135]
4. Zhang Y, Patil RV & Marmorstein AD Bestrophin 2 is expressed in human non-pigmented ciliary epithelium but not retinal pigment epithelium. Mol Vis 16, 200–206, (2010). [PubMed: 20157619]
5. Johnson AA et al. Bestrophin 1 and retinal disease. Progress in retinal and eye research, doi:10.1016/j.preteyeres.2017.01.006 (2017).
6. Lee S. et al. Channel-mediated tonic GABA release from glia. Science 330, 790–796, doi:10.1126/science.1184334 (2010). [PubMed: 20929730]
7. Li Y. et al. Patient-specific mutations impair BESTROPHIN1's essential role in mediating Ca2+-dependent Cl- currents in human RPE. Elife 6, doi:10.7554/eLife.29914 (2017).
8. Heijl A, Leske MC, Bengtsson B, Hyman L. & Hussein M. Reduction of intraocular pressure and glaucoma progression: results from the Early Manifest Glaucoma Trial. Arch Ophthalmol 120, 1268–1279, doi:ecs20122 (2002). [PubMed: 12365904]
9. Kass MA et al. The Ocular Hypertension Treatment Study: a randomized trial determines that topical ocular hypotensive medication delays or prevents the onset of primary open-angle glaucoma. Arch Ophthalmol 120, 701–713; discussion 829–730, doi:ecs20045 (2002). [PubMed: 12049574]
10. Lichter PR et al. Interim clinical outcomes in the Collaborative Initial Glaucoma Treatment Study comparing initial treatment randomized to medications or surgery. Ophthalmology 108, 1943–1953, doi:S0161–6420(01)00873–9 (2001). [PubMed: 11713061]
11. Owji AP et al. Structural and functional characterization of the bestrophin-2 anion channel. Nature structural & molecular biology 27, 382–391, doi:10.1038/s41594-020-0402-z (2020).
12. Qu Z, Fischmeister R. & Hartzell C. Mouse bestrophin-2 is a bona fide Cl(−) channel: identification of a residue important in anion binding and conduction. J Gen Physiol 123, 327–340, doi:10.1085/jgp.200409031 (2004). [PubMed: 15051805]
13. Qu Z. & Hartzell HC Bestrophin Cl- channels are highly permeable to HCO3. American journal of physiology. Cell physiology 294, C1371–1377, doi:10.1152/ajpcell.00398.2007 (2008).
14. Yu K, Lujan R, Marmorstein A, Gabriel S. & Hartzell HC Bestrophin-2 mediates bicarbonate transport by goblet cells in mouse colon. J Clin Invest 120, 1722–1735, doi:10.1172/JCI41129 (2010). [PubMed: 20407206]
15. Han KS et al. Channel-mediated astrocytic glutamate release via Bestrophin-1 targets synaptic NMDARs. Mol Brain 6, 4, doi:10.1186/1756-6606-6-4 (2013). [PubMed: 23324492]
16. Jo S. et al. GABA from reactive astrocytes impairs memory in mouse models of Alzheimer's disease. Nature medicine 20, 886–896, doi:10.1038/nm.3639 (2014).
17. Koh W. et al. Astrocytes Render Memory Flexible by Releasing D-Serine and Regulating NMDA Receptor Tone in the Hippocampus. Biological psychiatry 91, 740–752, doi:10.1016/j.biopsych.2021.10.012 (2022). [PubMed: 34952697]
18. Kwak H. et al. Astrocytes Control Sensory Acuity via Tonic Inhibition in the Thalamus. Neuron 108, 691–706 e610, doi:10.1016/j.neuron.2020.08.013 (2020).
19. Oh SJ et al. Protease activated receptor 1-induced glutamate release in cultured astrocytes is mediated by Bestrophin-1 channel but not by vesicular exocytosis. Mol Brain 5, 38, doi:10.1186/1756-6606-5-38 (2012). [PubMed: 23062602]
20. Park H. et al. High glutamate permeability and distal localization of Best1 channel in CA1 hippocampal astrocyte. Mol Brain 6, 54, doi:10.1186/1756-6606-6-54 (2013). [PubMed: 24321245]
21. Woo DH et al. TREK-1 and Best1 channels mediate fast and slow glutamate release in astrocytes upon GPCR activation. Cell 151, 25–40, doi:10.1016/j.cell.2012.09.005 (2012). [PubMed: 23021213]
22. Kane Dickson V, Pedi L. & Long SB Structure and insights into the function of a Ca(2+)-activated Cl(−) channel. Nature 516, 213–218, doi:10.1038/nature13913 (2014). [PubMed: 25337878]

23. Owji AP et al. Structures and gating mechanisms of human bestrophin anion channels. Nature communications 13, 3836, doi:10.1038/s41467-022-31437-7 (2022).
24. Yang T. et al. Structure and selectivity in bestrophin ion channels. Science 346, 355–359, doi:10.1126/science.1259723 (2014). [PubMed: 25324390]
25. Miller AN, Vaisey G. & Long SB Molecular mechanisms of gating in the calcium-activated chloride channel bestrophin. Elife 8, doi:10.7554/eLife.43231 (2019).
26. Hu RG, Lim JC, Kalloniatis M. & Donaldson PJ Cellular localization of glutamate and glutamine metabolism and transport pathways in the rat ciliary epithelium. Investigative ophthalmology & visual science 52, 3345–3353, doi:10.1167/iovs.10-6422 (2011). [PubMed: 21593199]
27. Langford MP et al. Apical localization of glutamate in GLAST-1, glutamine synthetase positive ciliary body nonpigmented epithelial cells. Clin Ophthalmol 1, 43–53 (2007). [PubMed: 19668465]
28. Hu RG, Zhu Y, Donaldson P. & Kalloniatis M. Alterations of glutamate, glutamine, and related amino acids in the anterior eye secondary to ischaemia and reperfusion. Curr Eye Res 37, 633–643, doi:10.3109/02713683.2012.669509 (2012). [PubMed: 22587229]
29. Moreno MC et al. Effect of glaucoma on the retinal glutamate/glutamine cycle activity. FASEB J 19, 1161–1162, doi:10.1096/fj.04-3313fje (2005). [PubMed: 15870062]
30. Krajewski WW et al. Crystal structures of mammalian glutamine synthetases illustrate substrate-induced conformational changes and provide opportunities for drug and herbicide design. J Mol Biol 375, 217–228, doi:10.1016/j.jmb.2007.10.029 (2008). [PubMed: 18005987]
31. Yu DY, Noh SM & Lee GM Limitations to the development of recombinant human embryonic kidney 293E cells using glutamine synthetase-mediated gene amplification: Methionine sulfoximine resistance. J Biotechnol 231, 136–140, doi:10.1016/j.jbiotec.2016.06.003 (2016). [PubMed: 27288593]
32. Ji C. et al. Dual Ca(2+)-dependent gates in human Bestrophin1 underlie disease-causing mechanisms of gain-of-function mutations. Commun Biol 2, 240, doi:10.1038/s42003-019-0433-3433 [pii] (2019). [PubMed: 31263784]
33. Zhang Y. et al. ATP activates bestrophin ion channels through direct interaction. Nature communications 9, 3126, doi:10.1038/s41467-018-05616-4 (2018).
34. Rivas S, Hanif K, Chakouri N. & Ben-Johny M. Probing ion channel macromolecular interactions using fluorescence resonance energy transfer. Methods in enzymology 653, 319–347, doi:10.1016/bs.mie.2021.01.047 (2021). [PubMed: 34099178]
35. Kittredge A, Ward N, Hopiavuori A, Zhang Y. & Yang T. Expression and Purification of Mammalian Bestrophin Ion Channels. J Vis Exp, doi:10.3791/57832 (2018).
36. Ji C. et al. Investigation and Restoration of BEST1 Activity in Patient-derived RPEs with Dominant Mutations. Scientific reports 9, 19026, doi:10.1038/s41598-019-54892-7 (2019).
37. Zhao Q. et al. Distinct expression requirements and rescue strategies for BEST1 loss- and gain-of-function mutations. Elife 10, doi:10.7554/eLife.67622 (2021).
38. Zheng SQ et al. MotionCor2: anisotropic correction of beam-induced motion for improved cryo-electron microscopy. Nature methods 14, 331–332, doi:nmeth.4193 [pii] 10.1038/nmeth.4193 (2017). [PubMed: 28250466]
39. Zivanov J, Nakane T. & Scheres SHW A Bayesian approach to beam-induced motion correction in cryo-EM single-particle analysis. IUCrJ 6, 5–17, doi:10.1107/S205225251801463X (2019).
40. Punjani A, Zhang H. & Fleet DJ Non-uniform refinement: adaptive regularization improves single-particle cryo-EM reconstruction. Nature methods 17, 1214–1221, doi:10.1038/s41592-020-00990-8 (2020). [PubMed: 33257830]
41. Waterhouse A. et al. SWISS-MODEL: homology modelling of protein structures and complexes. Nucleic Acids Res 46, W296–W303, doi:10.1093/nar/gky427 (2018). [PubMed: 29788355]
42. Emsley P. & Cowtan K. Coot: model-building tools for molecular graphics. Acta Crystallogr D Biol Crystallogr 60, 2126–2132, doi:10.1107/S0907444904019158 (2004). [PubMed: 15572765]
43. Afonine PV et al. Real-space refinement in PHENIX for cryo-EM and crystallography. Acta crystallographica. Section D, Structural biology 74, 531–544, doi:10.1107/S2059798318006551 (2018). [PubMed: 29872004]

44. Chen VB et al. MolProbity: all-atom structure validation for macromolecular crystallography. Acta Crystallogr D Biol Crystallogr 66, 12–21, doi:10.1107/S0907444909042073 (2010). [PubMed: 20057044]

45. Afonine PV et al. New tools for the analysis and validation of cryo-EM maps and atomic models. Acta crystallographica. Section D, Structural biology 74, 814–840, doi:10.1107/S2059798318009324 (2018). [PubMed: 30198894]

46. Barad BA et al. EMRinger: side chain-directed model and map validation for 3D cryo-electron microscopy. Nature methods 12, 943–946, doi:10.1038/nmeth.3541 (2015). [PubMed: 26280328]

47. Pintilie G. et al. Measurement of atom resolvability in cryo-EM maps with Q-scores. Nature methods 17, 328–334, doi:10.1038/s41592-020-0731-1 (2020). [PubMed: 32042190]

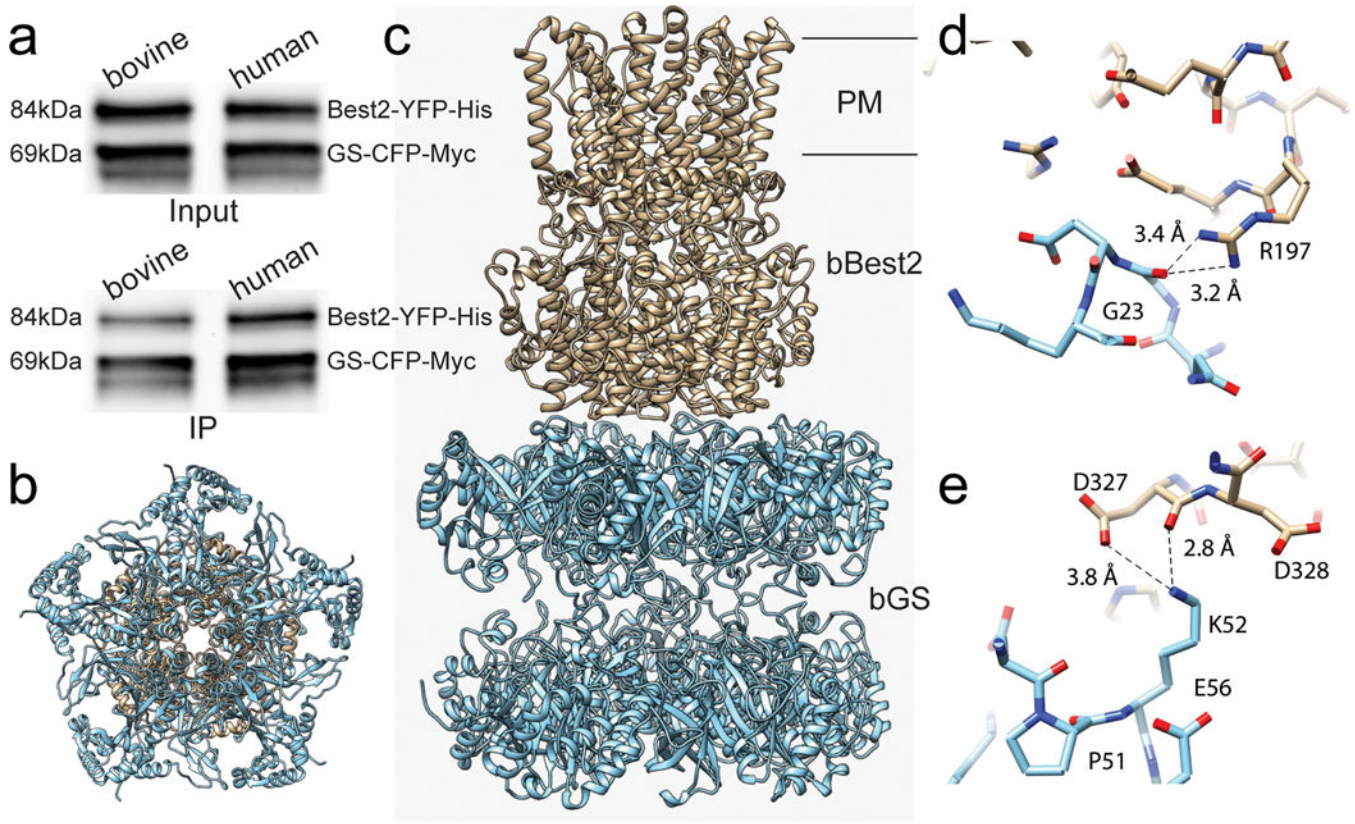

Figure 1. Complex formation between Best2 and GS.

(**a**) Co-expressed Best2-YFP-His and GS-CFP-Myc were detected by immunoblotting in input (*top*) and co-immunoprecipitation (*bottom*) samples. (**b, c**) Ribbon diagrams of the bovine Best2-GS cryo-EM structure model from the bottom (**b**) and side (**c**) views. bBest2 and bGS are labeled with tan and blue, respectively; one pentamer of the bGS decamer was removed to make the interface easier to see in **b**; PM, plasma membrane. (**d, e**) Stick diagram showing the interaction between G23 of bGS and R197 of bBest2 (**d**), and the salt bridges formed between K52 of bGS and D327 of bBest2 (**e**). Black lines illustrate distance.

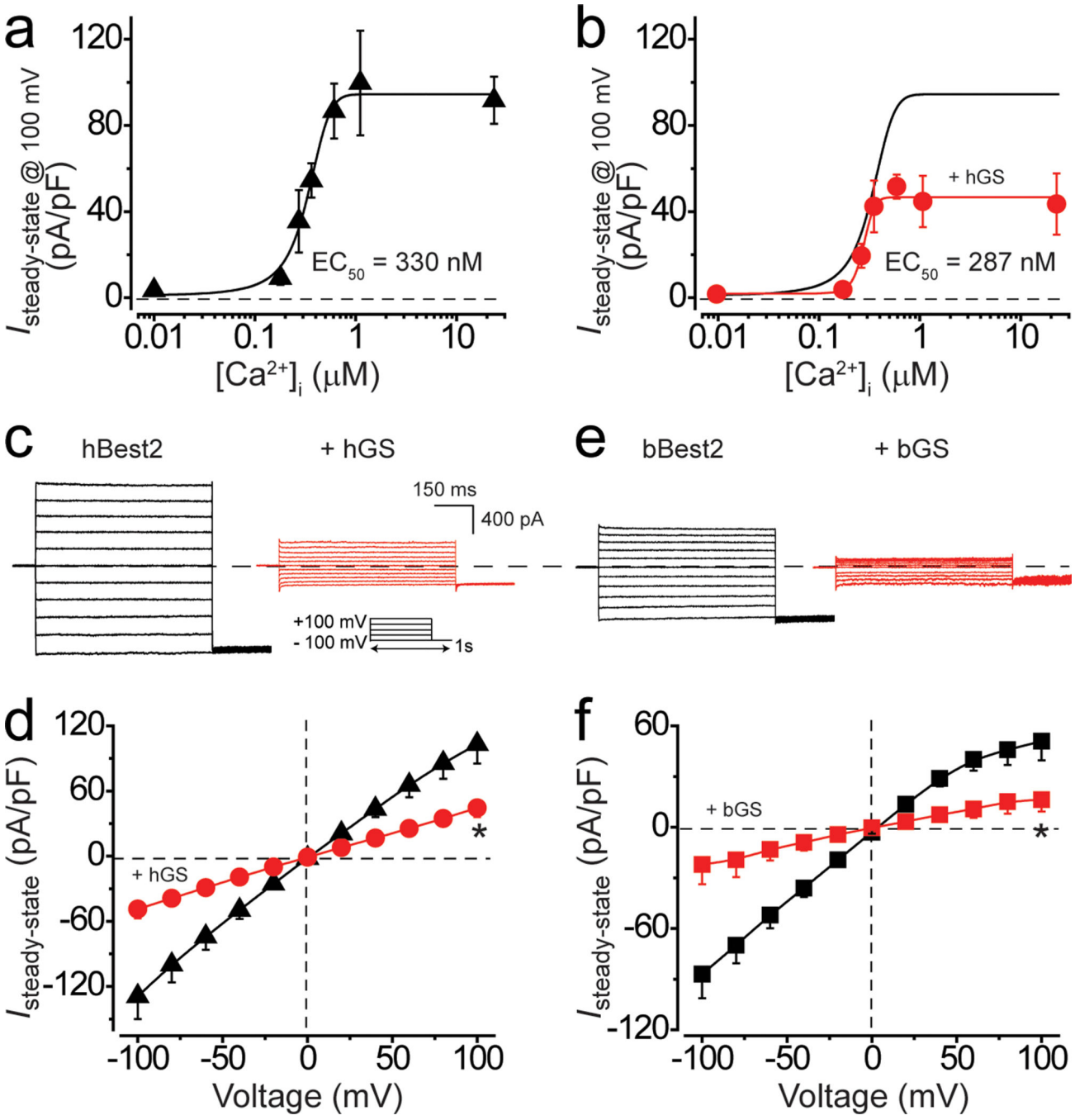

Figure 2. Influence of GS on Best2 function in HEK293 cells.

(**a**) Ca^{2+}-dependent Cl^- currents conducted by hBest2. Steady-state current density was recorded at +100 mV plotted vs. $[Ca^{2+}]_i$ and fitted to the Hill equation; n = 7. (**b**) Ca^{2+}-dependent Cl^- currents from hBest2 with (red, n=7) or without (black, n = 7) hGS. Steady-state current density was recorded at +100 mV plotted vs. $[Ca^{2+}]_i$ and fitted to the Hill equation. (**c, d**) Representative current traces (**c**) and population steady-state current density-voltage relationships (**d**) of hBest2 without (black, n = 9) or with hGS (red, n = 5) at 1 μM $[Ca^{2+}]_i$; **p* = 0.04 compared to hBest2 alone; *Inset*, voltage protocol used to

elicit currents. (**e, f**) Representative current traces (**e**) and population steady-state current density-voltage relationships (**f**) of bBest2 without (black, n = 10) or with bGS (red, n = 6) at 1 μM $[Ca^{2+}]_i$; **p* = 0.047 compared to bBest2 alone. All error bars are presented as mean values +/− SEM; *p* values are calculated by two-tailed unpaired Student's *t* test.

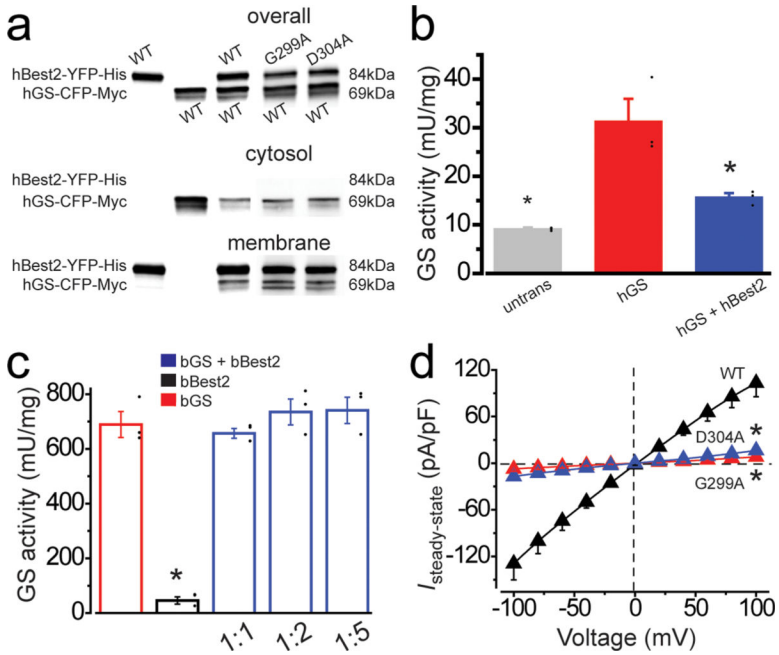

Figure 3. Influence of Best2 on GS function.

(**a**) The overall, cytosolic and membrane-bound levels of hBest2 and hGS in transiently transfected HEK293 cells. (**b**) Bar chart showing cytosolic GS activities in HEK293 cells transiently transfected with the indicated constructs; n = 3; **p* = 9E-3 and 0.03 for untransfected and hGS + hBest2 co-transfected cells, respectively, compared to cells transfected with hGS alone. (**c**) Bar chart showing GS activity measured with purified bGS and bBest2 proteins; n = 3; **p* = 2E-4 compared to bGS alone. (**d**) Population steady-state current density-voltage relationships of hBest2 mutants (G299A, red, n = 5; D304A, blue, n = 6) compared to WT hBest2 (black, n = 9) at 1 μM $[Ca^{2+}]_i$ in transiently transfected HEK293 cells; **p* = 2E-3 for both D304A and G299A, compared to WT hBest2. All error bars are presented as mean values +/− SEM; *p* values are calculated by two-tailed unpaired Student's *t* test.

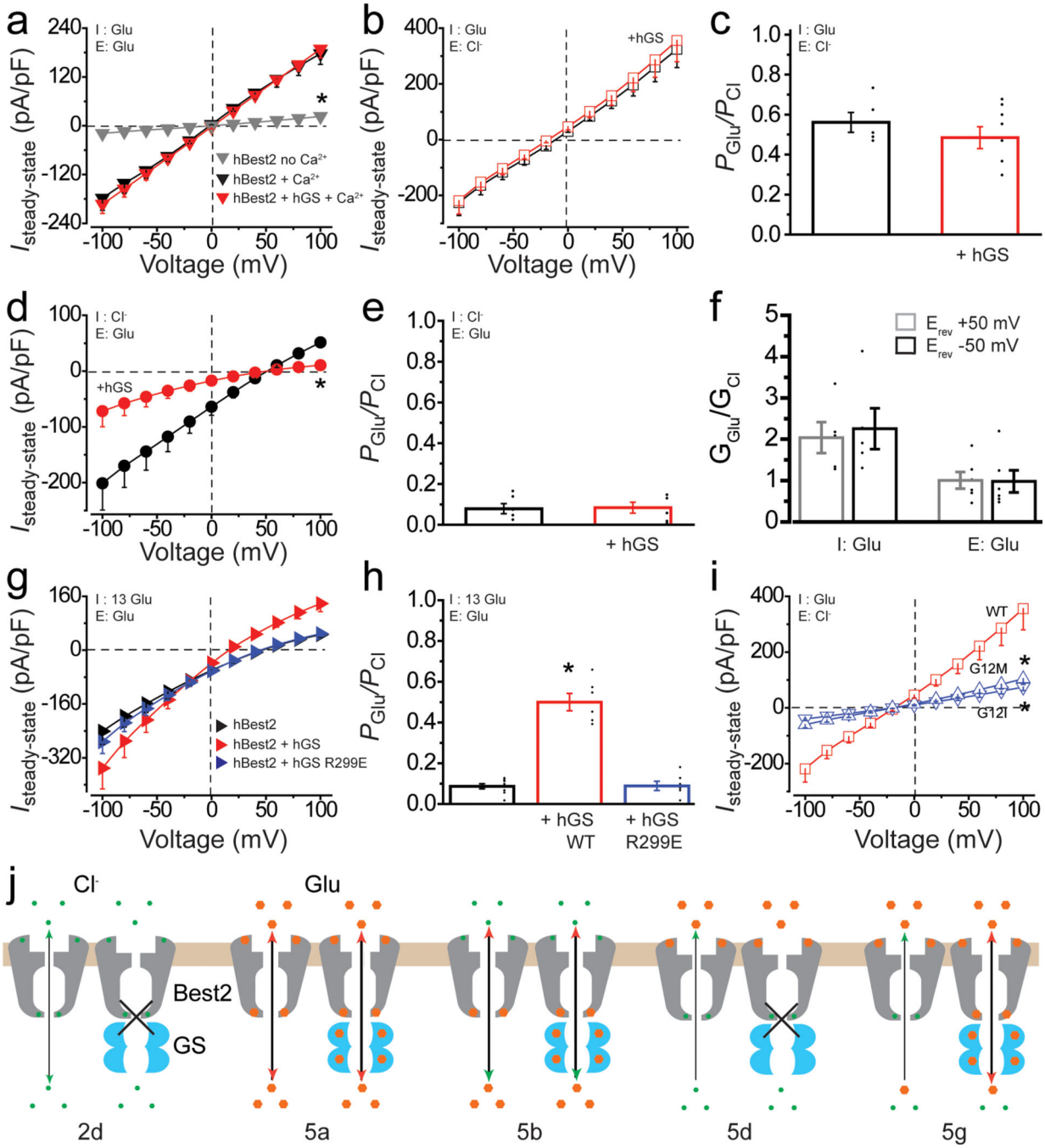

Figure 4. Permeability of hBest2-GS to glutamate in HEK293 cells.

(**a**) I-V relationships of hBest2 alone in the absence (gray, n = 7) or presence (black, n = 9) of 1 μM $[Ca^{2+}]_i$ compared to hBest2 + hGS at 1 μM $[Ca^{2+}]_i$ (red, n = 7), with glutamate as the principal anion; *p = 2E-4 compared to hBest2 alone with Ca^{2+}. (**b, c**) I-V relationships (**b**) and glutamate to Cl^- relative permeability ratios (**c**) of hBest2 in the absence (black, n = 5) or presence (red, n = 8) of hGS at 1 μM $[Ca^{2+}]_i$ with internal glutamate and external Cl^-. (**d, e**) The same format as **b, c**, respectively, but with external glutamate and internal Cl^-; n = 6 for both groups; *p = 5E-4 compared to hBest2 alone. (**f**) Relative ion conductance ratios

(G_{Glu}/G_{Cl}) of hBest2 at 1 μM $[Ca^{2+}]_i$; n = 5 and 6 for the internal and external glutamate group, respectively. (**g, h**) The same format as **d, e**, but with 13 mM internal Cl^- substituted by glutamate; n = 9, 6 and 6 for hBest2 alone, hBest2 + WT hGS and hBest2 + hGS R299E, respectively; *p = 6E-8 compared to hBest2 alone. (**i**) I-V relationships of hBest2 in the presence of WT (red, n = 8) or mutant (blue, n = 9 and 11 for G12I and G12M, respectively) hGS at 1 μM $[Ca^{2+}]_i$ with internal glutamate and external Cl^-; *p = 1E-3 and 2E-3 for G12I and G12M, respectively, compared to WT GS. (**j**) Cartoon showing the effect of GS on Best2-mediated Cl^-/glutamate permeation, labeled with the corresponding panel of each scenario underneath. The glutamate binding sites on Best2 are speculative. All error bars are presented as mean values +/− SEM; p values are calculated by two-tailed unpaired Student's t test.

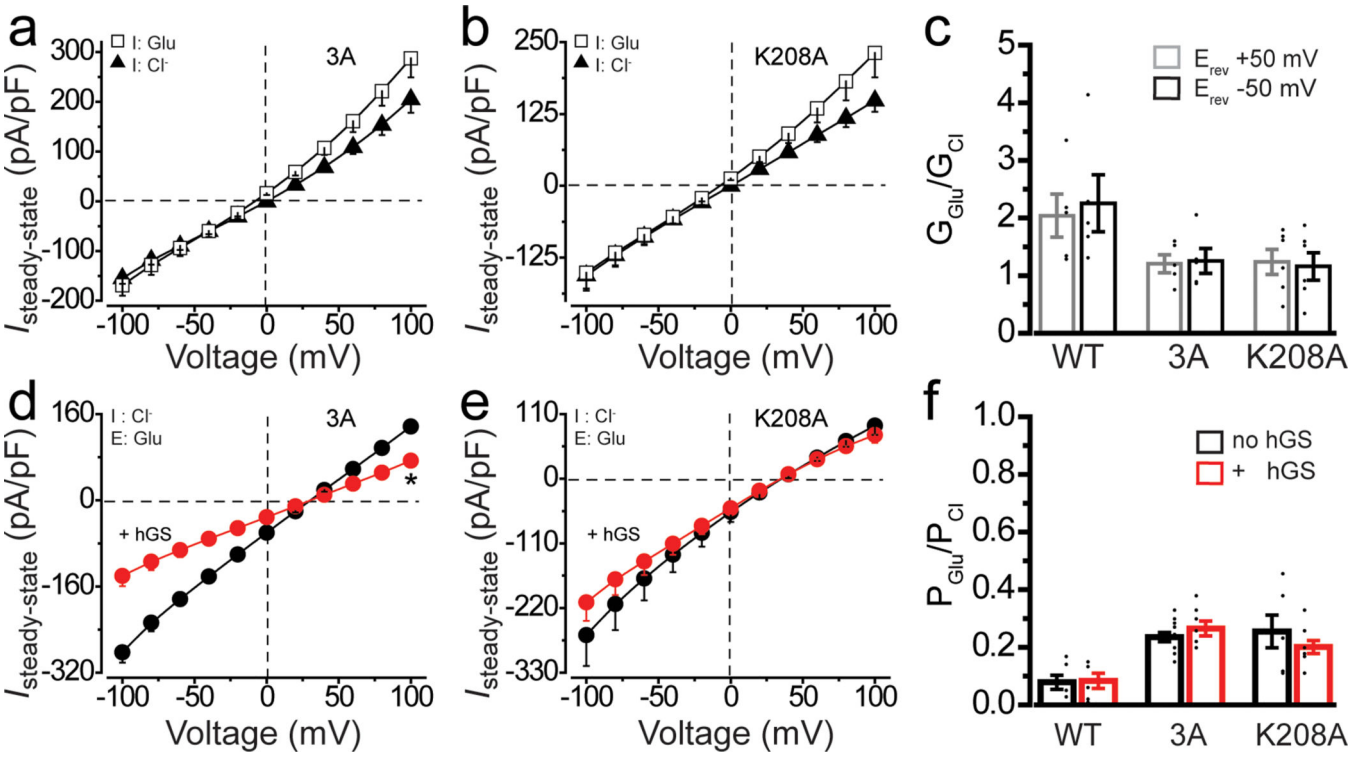

Figure 5. Roles of the neck and aperture in glutamate permeability and GS-mediated inhibition.

(**a, b**) Population steady-state current density-voltage relationships of hBest2 3A (**a**) and K208A (**b**) mutants in the presence of 1 μM $[Ca^{2+}]_i$ in transiently transfected HEK293 cells with internal glutamate (open square) or Cl^- (solid triangle) and external Cl^- as the principal anions; n = 5 for 3A under both conditions, and n = 8 and 6 for K208A with internal Cl^- and glutamate, respectively. (**c**) Relative ion conductance ratios (G_{Glu}/G_{Cl}) of hBest2 WT (n = 5), 3A (n = 5) and K208A (n = 6) at 1 μM $[Ca^{2+}]_i$. (**d, e**) Population steady-state current density-voltage relationships of hBest2 3A (**d**) and K208A (**e**) mutants in the absence (black) or presence of hGS (red) at 1 μM $[Ca^{2+}]_i$ in transiently transfected HEK293 cells with internal Cl^- and external glutamate as the principal anions; n = 12 and 7 for 3A without or with GS, respectively, and n = 6 and 8 for K208A without or with GS, respectively; **p* = 8E-5 compared to hBest2–3A alone by two-tailed unpaired Student's *t* test. (**f**) Relative ion permeability ratios of glutamate to Cl^- (P_{Glu}/P_{Cl}) on hBest2 in the absence (black) or presence (red) of GS, calculated using data from **d**, **e** and **4d**. All error bars are presented as mean values +/− SEM.

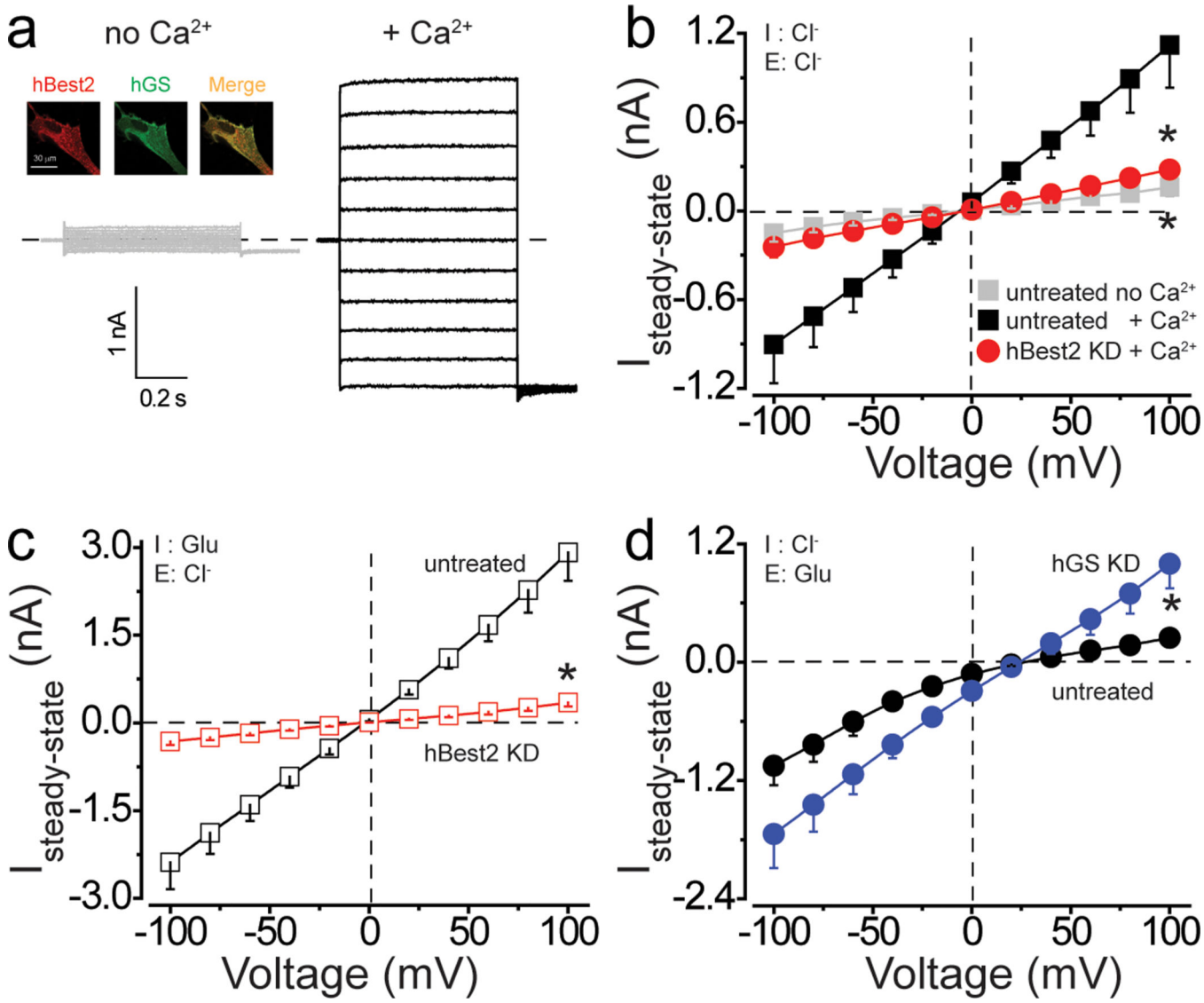

Figure 6. Influence of hGS on hBest2-mediated Ca^{2+}-dependent anion currents in human NPE cells.

(**a**) Representative current traces in cells without (gray) or with (black) 1 μM $[Ca^{2+}]_i$. *Inset*, confocal images showing the subcellular co-localization of endogenous hBest2 and hGS in NPE detected by immunostaining. (**b**) Population steady-state current-voltage relationships in cells with (red, n = 5) or without (black, n = 8) siRNA-mediated hBest2 knockdown at 1 μM $[Ca^{2+}]_i$ and untreated cells without Ca^{2+} (gray, n = 6), with Cl^- as the principal internal and external anion. *p = 0.02 and 0.04 for the no Ca^{2+} and hBest2 knockdown group, respectively, compared to untreated cells with Ca^{2+}. (**c**) Population steady-state current-voltage relationships in cells with (red, n = 5) or without (black, n = 10) siRNA-mediated hBest2 knockdown at 1 μM $[Ca^{2+}]_i$, with internal glutamate and external Cl^- as the principal anions. *p = 3E-3 compared to currents from cells without hBest2 knockdown. (**d**) Population steady-state current-voltage relationships in cells with (blue, n = 7) or without (black, n = 5) siRNA-mediated hGS knockdown at 1 μM $[Ca^{2+}]_i$, with external glutamate

and internal Cl^- as the principal anions. *$p = 0.03$ compared to currents from cells without hGS knockdown. All error bars are presented as mean values +/− SEM; p values are calculated by two-tailed unpaired Student's t test.